The Astrophysical Journal, 760:107 (16pp), 2012 December 1 doi:10.1088/0004-637X/760/2/107

INFRARED STUDY OF FULLERENE PLANETARY NEBULAE

D. A. García-Hernández[1,2], E. Villaver[3], P. García-Lario[4], J. A. Acosta-Pulido[1,2], A. Manchado[1,2,5], L. Stanghellini[6], R. A. Shaw[6], and F. Cataldo[7,8]
[1] Instituto de Astrofísica de Canarias, C/Via Láctea s/n, E-38205 La Laguna, Spain; agarcia@iac.es, amt@iac.es
[2] Departamento de Astrofísica, Universidad de La Laguna (ULL), E-38206 La Laguna, Spain
[3] Departamento de Física Teórica, Universidad Autónoma de Madrid, E-28049 Madrid, Spain; eva.villaver@uam.es
[4] Herschel Science Centre, European Space Astronomy Centre, Research and Scientific Support Department of ESA, Villafranca del Castillo, P.O. Box 78, E-28080 Madrid, Spain; Pedro.Garcia-Lario@sciops.esa.int
[5] Consejo Superior de Investigaciones Científicas, Madrid, Spain
[6] National Optical Astronomy Observatory, 950 North Cherry Avenue, Tucson, AZ 85719, USA; shaw@noao.edu, letizia@noao.edu
[7] Istituto Nazionale di Astrofisica—Osservatorio Astrofisico di Catania, Via S. Sofia 78, I-95123 Catania, Italy; franco.cataldo@fastwebnet.it
[8] Actinium Chemical Research, Via Casilina 1626/A, I-00133 Rome, Italy
Received 2012 August 4; accepted 2012 September 29; published 2012 November 9

ABSTRACT

We present a study of 16 planetary nebulae (PNe) where fullerenes have been detected in their *Spitzer Space Telescope* spectra. This large sample of objects offers a unique opportunity to test conditions of fullerene formation and survival under different metallicity environments because we are analyzing five sources in our own Galaxy, four in the Large Magellanic Cloud (LMC), and seven in the Small Magellanic Cloud (SMC). Among the 16 PNe studied, we present the first detection of C_{60} (and possibly also C_{70}) fullerenes in the PN M 1−60 as well as of the unusual ∼6.6, 9.8, and 20 μm features (attributed to possible planar C_{24}) in the PN K 3−54. Although selection effects in the original samples of PNe observed with *Spitzer* may play a potentially significant role in the statistics, we find that the detection rate of fullerenes in C-rich PNe increases with decreasing metallicity (∼5% in the Galaxy, ∼20% in the LMC, and ∼44% in the SMC) and we interpret this as a possible consequence of the limited dust processing occurring in Magellanic Cloud (MC) PNe. *CLOUDY* photoionization modeling matches the observed IR fluxes with central stars that display a rather narrow range in effective temperature (∼30,000–45,000 K), suggesting a common evolutionary status of the objects and similar fullerene formation conditions. Furthermore, the data suggest that fullerene PNe likely evolve from low-mass progenitors and are usually of low excitation. We do not find a metallicity dependence on the estimated fullerene abundances. The observed C_{60} intensity ratios in the Galactic sources confirm our previous finding in the MCs that the fullerene emission is not excited by the UV radiation from the central star. *CLOUDY* models also show that line- and wind-blanketed model atmospheres can explain many of the observed [Ne III]/[Ne II] ratios using photoionization, suggesting that possibly the UV radiation from the central star, and not shocks, is triggering the decomposition of the circumstellar dust grains. With the data at hand, we suggest that the most likely explanation for the formation of fullerenes and graphene precursors in PNe is that these molecular species are built from the photochemical processing of a carbonaceous compound with a mixture of aromatic and aliphatic structures similar to that of hydrogenated amorphous carbon dust.

Key words: astrochemistry – circumstellar matter – infrared: stars – planetary nebulae: general – stars: AGB and post-AGB

Online-only material: color figures

1. INTRODUCTION

The existence of fullerenes, highly resistant molecules formed exclusively by carbon atoms numbering 60 and more, was predicted in the 1970s as a possible variety of carbon assemblage in the universe (Osawa 1970). However, it was only in the 1980s when the most common fullerenes C_{60} (buckyball) and C_{70} were synthesized in the laboratory for the first time (Kroto et al. 1985) in an effort to trace the carriers of the elusive diffuse interstellar bands. Since then, they have been found on Earth (e.g., Buseck et al. 1992), on meteorites (e.g., Becker et al. 1999),[9] in planetary nebulae (PNe; Cami et al. 2010; García-Hernández et al. 2010, 2011a), and in the interstellar medium (ISM; Sellgren et al. 2010). More recently, fullerenes have also been detected in a proto-planetary nebula (Zhang & Kwok 2011), around R Coronae Borealis (RCB) stars (García-Hernández et al. 2011b, 2011c), in the Orion Nebula (Rubin et al. 2011), in post-asymptotic giant branch (AGB) circumbinary disks (Gielen et al. 2011), in young stellar objects (YSOs), and around a Herbig Ae/Be star (Roberts et al. 2012).

From the variety of environments where fullerene molecules have been recently detected, the picture is emerging that the conditions for fullerene formation cannot be too stringent since they have to be shared by star-forming regions, evolved stars, and the ISM. In that sense, the detection by the *Spitzer Space Telescope* of fullerenes in a remarkably large number of PNe (16 sources so far)[10] offers a unique opportunity to test the conditions of fullerene formation and survival.

PNe represent the evolutionary stage during which the slow, intense dust-driven winds, which are the signature of the late AGB evolution, become ionized. During the PN phase, the

[9] Note that the fullerene detections on Earth and meteorites are somewhat controversial and it is not certain that these authors have really found fullerenes in their matrices.

[10] Note that instead, fullerenes have been detected toward a few—sometimes even only one—targets in other astrophysical environments, such as RCB stars, YSOs, etc.

effective temperature of the central star can reach 200,000 K, while a fast, low-density post-AGB wind, shocks and shapes the inner parts of the previously ejected AGB envelope. Chemically, the envelope shredded from the AGB star can show a C-rich or O-rich chemistry, primarily as a direct consequence of the number and efficiency of dredge-up processes experienced by the central star. These processes ultimately are just determined by the stellar initial mass and its evolutionary stage (Herwig 2005). Dynamically, the evolution of the shocked ejected shell is mainly determined by both the stellar evolutionary stage and core mass (see, e.g., Villaver et al. 2002a, 2002b). In addition, during the PN phase, two fundamental chemical drivers the UV radiation field from the central star and the shocks generated by the stellar winds, are present and quickly evolving (see, e.g., Kwok 2004).

From laboratory experiments, we can learn a lot about the formation process of fullerenes (Kroto et al. 1985; Kratschmer et al. 1990; de Vries et al. 1993) and the first synthesis of fullerenes in the lab motivated the first searches in space. However, they can also be misleading. Although the laboratory synthesis of fullerenes shows that they are more efficiently produced under hydrogen-deficient conditions, this does not seem to be the case in space, where fullerenes seem to be efficiently formed in H-rich circumstellar environments (García-Hernández et al. 2010, 2011a). This is manifested by the presence of C_{60} fullerene bands in *Spitzer* spectra of Galactic and extra-Galactic PNe with normal H-rich central stars that also display the classical aromatic infrared bands (AIBs) usually attributed to polycyclic aromatic hydrocarbons (PAHs; García-Hernández et al. 2010, 2011a), including the PN Tc 1. Interestingly, fullerenes have been detected in PNe, whose IR spectra are clearly dominated by aliphatic C-rich dust, represented by broad emissions such as those centered at ∼6–9, 9–13, 15–20, and 25–35 μm.[11] The different spectral properties of these broad features observed from source to source are quite consistent with the expected differing properties of the hydrogenated amorphous carbon (HAC) grains (or their decomposition products), which may be present in the circumstellar envelopes of these stars. That would explain the wide range of different spectra observed, depending on their physical and chemical properties (e.g., size, shape, and degree of hydrogenation; see García-Hernández et al. 2010, 2011a). This raises the exciting possibility that considerable physical and chemical processing of dust occurs just after the AGB phase (see also Zhang & Kwok 2011), including the formation of fullerenes. Moreover, fullerenes, being relatively hardy molecules, may survive indefinitely in space, playing an important role in circumstellar/interstellar chemistry and physics.

From the experimental point of view, laboratory spectroscopy of C_{60} and C_{70} fullerenes (Iglesias-Groth et al. 2011) only very recently has provided the temperature dependence of wavelength shifts and molar absorptivity of the C_{60} and C_{70} infrared bands, which are fundamental for a firm identification of the observed bands as fullerenes and for a quantitative abundance determination of these molecules in space.

In this paper, we present a study of the infrared properties of 16 fullerene PNe, including the first detection of fullerenes in the Galactic PN M 1−60 and of the unusual ∼6.6, 9.8, and 20 μm features (attributed to possible planar C_{24}) in the PN K 3−54. Our sample represents the largest (irrespective of object type) in which fullerene molecules have been detected and includes for the first time objects belonging to very different metallicity environments (the Galaxy and the Large and Small Magellanic Clouds (LMC and SMC)), allowing the study of how metallicity influences the chemical route for fullerene formation. The *Spitzer* infrared data used in our study are described in Section 2, while the data analysis, including the estimation of C_{60} and C_{70} fullerene abundances, is presented in Section 3. Section 4 discusses the results of our study and we offer conclusions in Section 5.

[11] Note that the 15–20 μm emission may be also related with the C–C–C bending modes of relatively large PAHs or PAH clusters (e.g., Van Kerckhoven et al. 2000).

2. DATA

We searched for the presence of the infrared features attributed to the C_{60} and C_{70} molecules in the spectra of a large sample of PNe (mainly from our own *Spitzer* programs) and available in the *Spitzer*/IRS archive. This includes the infrared spectra obtained under *Spitzer* GO programs 3633 (P.I.: M. Bobrowsky) and 20443 and 50261 (P.I.: L. Stanghellini). A total of 238 *Spitzer*/IRS spectra of PNe were obtained under these programs with the general goal of investigating the chemical properties and dust evolution during this evolutionary stage and are published elsewhere in studies dealing with the original goals as proposed to the *Spitzer* observatory. All *Spitzer* programs have in common spectral coverage in the ∼5–38 μm range, making use of different combinations of the short–low (SL: 5.2–14.5 μm; $64 < R < 128$), long–low (LL: 14.0–38 μm; $64 < R < 128$), short–high (SH: 9.9–19.6 μm; $R \sim 600$), and long–high (LH: 18.7–37.2 μm; $R \sim 600$) modules depending on the source brightness in the mid-IR.[12] Detailed descriptions of observations and the data reduction process can be found in Perea-Calderón et al. (2009) (program 3633) for the 40 PNe observed in the Galactic Bulge, in Stanghellini et al. (2007) and Shaw et al. (2010) (program 20443) for the 41 PNe in the Magellanic Clouds (MCs), and in Stanghellini et al. (2012) (program 50261) for the 157 compact PNe observed in the Galactic disk. An additional sample of 25 PNe in the MCs was observed under GTO program 103 (see Bernard-Salas et al. 2009) and we included these data in the analysis as well. In summary, a total of 263 PNe are used in this paper in the search for fullerene emission and in the following analysis of its emission characteristics.

2.1. Spitzer/IRS Spectra of PNe with Fullerenes

The C_{60} fullerene molecule displays four infrared features located at ∼7.0, 8.5, 17.4, and 18.9 μm (e.g., Kratschmer et al. 1990; Iglesias-Groth et al. 2011). In order to better isolate these spectral features, we performed a careful subtraction of the dust continuum emission between 5 and 25 μm in the spectra of the 263 PNe mentioned above. To do so, the dust continuum emission was represented by 3–7 order polynomials fitted at spectral locations that we believed to be free from any dust or gas feature; for example, the spectral points at 6, 9, 14, and 24 μm are not affected by dust emission at 6–9, 9–13, 15–20, and 25–35 μm. Note that we preferred to exclude the 25–38 μm spectral region from the dust continuum subtraction because the 25–35 μm emission sometimes extends well beyond 38 μm, which made determining the location of the continuum difficult. Then, by inspecting the dust continuum subtracted or residual spectra, we searched for emission features at the four spectral positions corresponding to the bands that may be attributed to C_{60} fullerenes (see Figure 1). To illustrate the technique, in

[12] Note that a minimum S/N of ⩾50 is usually reached.

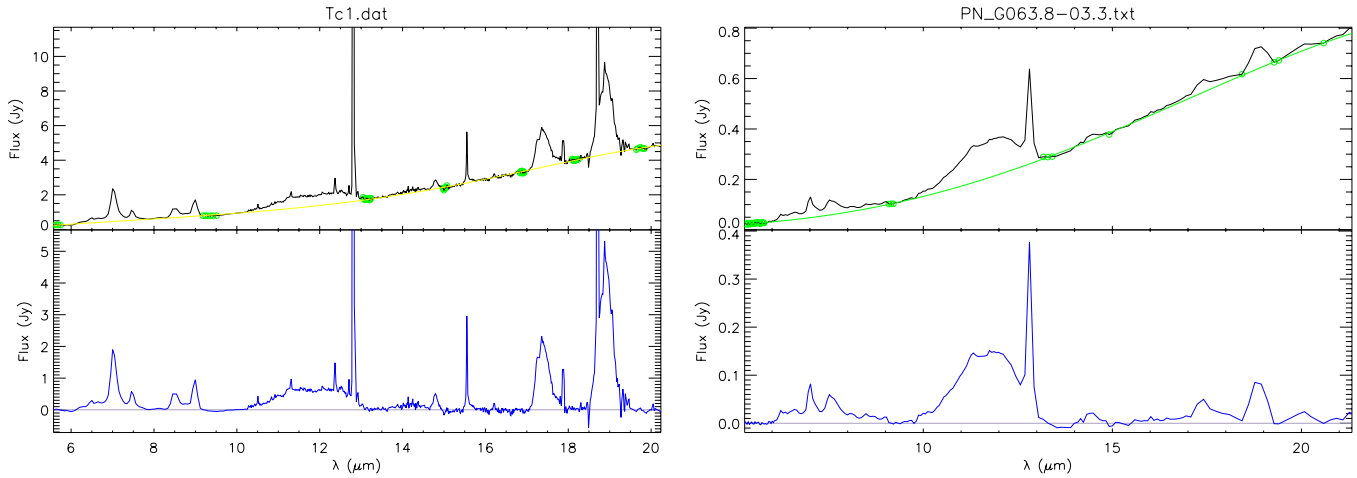

Figure 1. Illustrative examples of the polynomial fits made to the dust continuum and the corresponding residual spectra for the fullerene PNe Tc 1 (left panel) and K 3−54 (right panel). Both top panels show the observed *Spitzer*/IRS spectra (in black) together with a polynomial fit to continuum points free from any gas and dust feature. The corresponding residual or dust continuum subtracted spectra (in blue) are shown in the bottom panels.

(A color version of this figure is available in the online journal.)

Figure 1, we show examples of the dust continuum subtracted spectra of the PNe Tc 1 and K 3−54. Tc 1 (see the left panel in Figure 1) was observed at high resolution and displays some of the strongest fullerene features in our sample. On the other hand, PN K 3−54 (see the right panel in Figure 1) was observed at low resolution and displays much weaker fullerene bands than Tc 1.

We found obvious fullerene features in 16 objects out of the 263 PNe analyzed. They are distributed as follows: seven SMC PNe (six from program 20443 and one from program 103), four LMC PNe (three from program 20443 and one from program 103), and five Galactic PNe (three from program GO 3633 and two from program GO 50261). Most of these detections have already been published: three Galactic targets and one SMC target in García-Hernández et al. (2010); the 10 detections of fullerenes in PNe of the MCs in García-Hernández et al. (2011a); and the first fullerene detection in Tc 1 in Cami et al. (2010). In this paper, we report the detection of fullerenes in a new source, the Galactic PN M 1−60, and provide an overall and detailed analysis of the whole sample of PNe with fullerenes.

3. ANALYSIS

Figures 2–4 display the *Spitzer*/IRS spectra of all fullerene PNe discovered so far grouped by location or metallicity environment. We show in Figure 2 the targets in the Galaxy, while Figures 3 and 4 show the PNe in the LMC and SMC, respectively. Note that in these figures the strongest C_{60} feature at 18.9 μm (sometimes also C_{60} 17.4 μm) is distinctly present, superimposed on the dust continuum thermal emission. Most of the PNe also show broad dust emission features centered at ∼9–13 and/or 25–35 μm (the so-called 30 μm feature; e.g., Hrivnak et al. 2000). All C_{60}-detected PNe exhibit either the broad 30 μm or the 9–13 μm feature, but if not, then they display a very prominent 6–9 μm feature, like SMC 16 and SMC 24 (Figure 4), where this last feature is the strongest among the three features mentioned above. A huge 6–9 μm feature is also seen in LMC 02 (Figure 3), which does not show any 9–13 or 30 μm features. SMC 20 (Figure 4) is a peculiar case because it shows the strongest 9–13 and 15–20 μm features together while completely lacking the 30 μm feature.

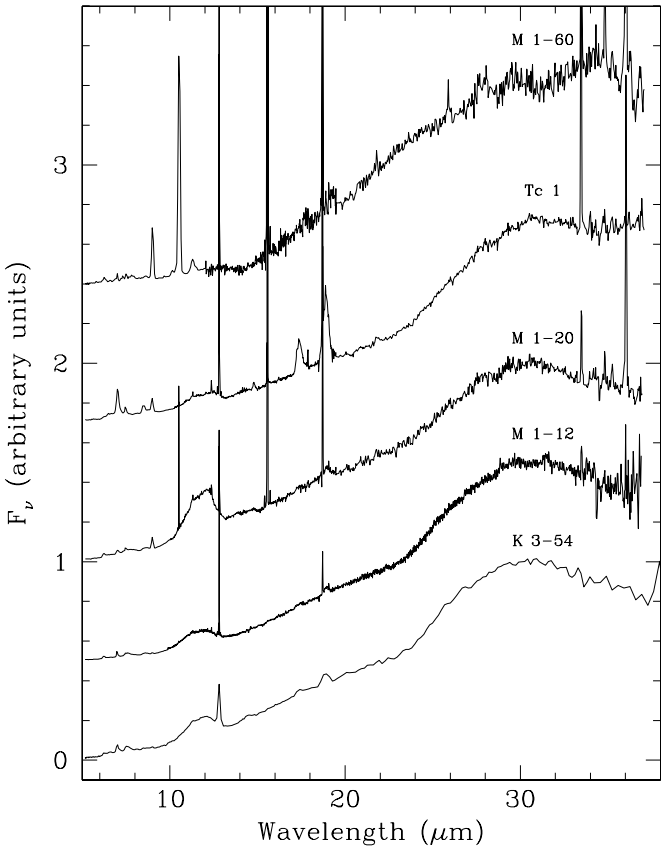

Figure 2. *Spitzer*/IRS spectra in the wavelength ∼5–38 μm for the five Galactic fullerene PNe in our sample. The spectra are normalized at 30 μm and the vertical axis has been artificially displaced for clarity. Note that the strongest C_{60} features at 17.4 and 18.9 μm are clearly superimposed on the dust continuum thermal emission.

M 1−60, a new fullerene PN[13], displays an extremely weak 9–13 μm feature together with a wider and sub-structured 30 μm feature—narrower (FWHM ∼ 0.5–3.5 μm) emission features superimposed to the broad 30 μm emission are seen at ∼25.9,

[13] M 1−60 also displays the weak AIBs at 6.2, 7.7, and 11.3 μm usually attributed to PAHs.

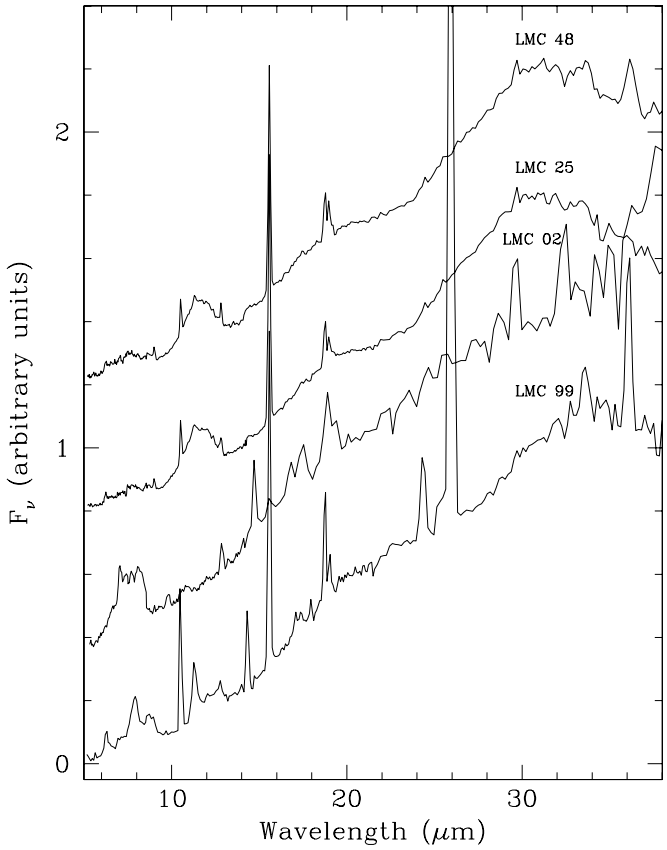

Figure 3. Same as Figure 2, but for the four Large MC PNe in our sample.

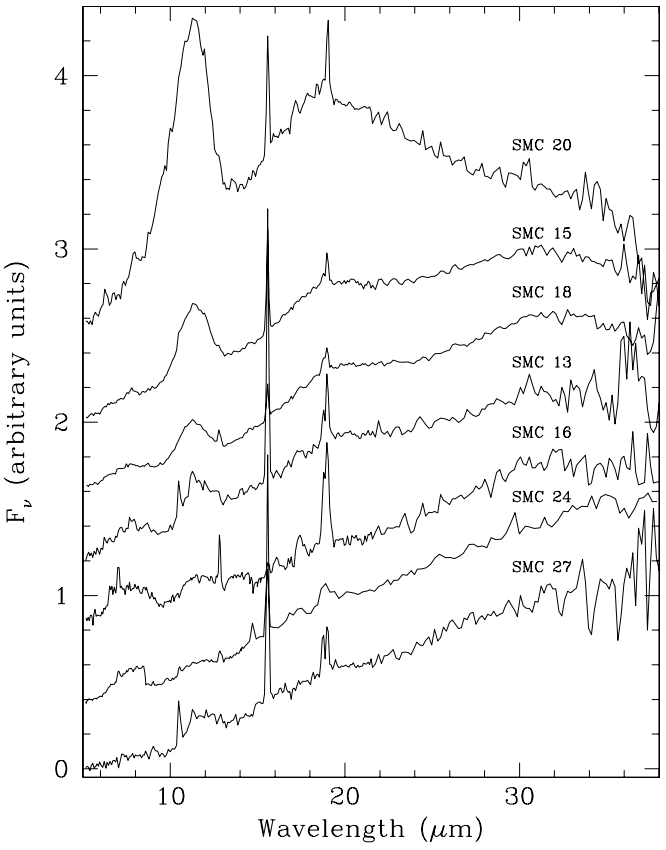

Figure 4. Same as Figure 2, but for the seven Small MC PNe in our sample.

27.8, 29.7, and 34.1 μm. The 30 μm feature seen in M 1−60 resembles that of the PPN IRAS 22574+6609 (Hrivnak et al. 2000), which also shows a narrow and unidentified emission feature at 25.8 μm. Interestingly, a similar pattern (although the features look weaker and narrower) of emission sub-features is also seen in other Galactic fullerene PNe such as Tc 1, M 1−20, and M 1−12 (Figure 2) for which high-resolution ($R \sim 600$) *Spitzer*/IRS spectra are available. We believe that these unidentified 30 μm sub-features are possibly related to the formation of fullerenes, in the sense that their carriers may be decomposition products of HACs (or a similar carbonaceus compound like coal, petroleum fractions, etc.) such as fullerene precursors.

It is worth noting here that the exact positions (and widths) of the ∼7.0, 8.5, 17.4, and 18.9 μm C_{60} features are temperature-dependent (see Iglesias-Groth et al. 2011, and references therein). Duley & Hu (2012) have very recently suggested that these four IR features may be due to proto-fullerenes rather than to C_{60} in objects that also show the 16.4 μm feature and other AIBs usually attributed to PAHs. The 16.4 μm feature is usually seen when the classical AIBs at 6.2, 7.7, and 11.3 μm are much stronger than the ∼7.0, 8.5, 17.4, and 18.9 μm IR features, as is the case for sources like reflection nebulae (NGC 7023 and NGC 2023), RCB stars (DY Cen and V854 Cen), the proto-PN IRAS 01005+7910, and a few post-AGB stars (Gielen et al. 2011). Thus, it is possible that the ∼7.0, 8.5, 17.4, and 18.9 μm IR features are due to proto-fullerenes in these sources (García-Hernández et al. 2012). However, the PN Tc 1 does not display strong AIBs or the 16.4 μm feature, which is a proxy for a source where only C_{60} fullerenes are detected. The 16.4 μm emission feature is not present in any of the PN sources analyzed in this paper, and the AIBs are very weak—contrary to the case in reflection nebulae, post-AGB stars, and RCB stars. Therefore, the most reasonable assumption is that the ∼7.0, 8.5, 17.4, and 18.9 μm emission features are mostly due to C_{60} fullerenes.

Some of the PNe in our sample (e.g., SMC 16, M 1−12, K 3−54, SMC 24, and LMC 02) are almost spectroscopic twins of Tc 1, showing the broad 6–9 and 9–13 μm emission plateaus 3 and 30 μm dust emission features characteristic of aliphatic hydrocarbons (see, e.g., Kwok & Zhang 2011) such as HAC aggregates or very small grains (VSGs; e.g., Tielens 2008). Thus, they should be in an evolutionary stage similar to Tc 1. This interpretation is supported by the narrow range of central star effective temperatures that all these sources have (see Section 3.1).

It is also important to consider that we lack the knowledge of the relative spatial distribution of the carrier of the AIBs with respect to C_{60} emission, which is an important aspect of the analysis and one that could offer important clues on the formation mechanism of fullerenes in PNe. The PNe are spatially small and the *Spitzer* spectrum generally encompasses the whole nebula. Tc 1 is the only exception, being the most extended source in our sample. In Tc 1, the fullerene and PAH emission seem to peak slightly offset from the central star (where the dust continuum emission peaks) and they look more extended by 1–2 pixels than the dust continuum emission. Indeed, a careful inspection of the Tc 1's *Spitzer* spectrum reveals the presence of very weak PAH 6.2 and 11.3 μm emission; see, e.g., Figures 2 and 3 in García-Hernández et al. (2010). Unfortunately, the *Spitzer*/IRS observations contain a marginal amount of information at a spatial resolution of ∼2″. We believe that mid-IR images at much higher spatial resolution

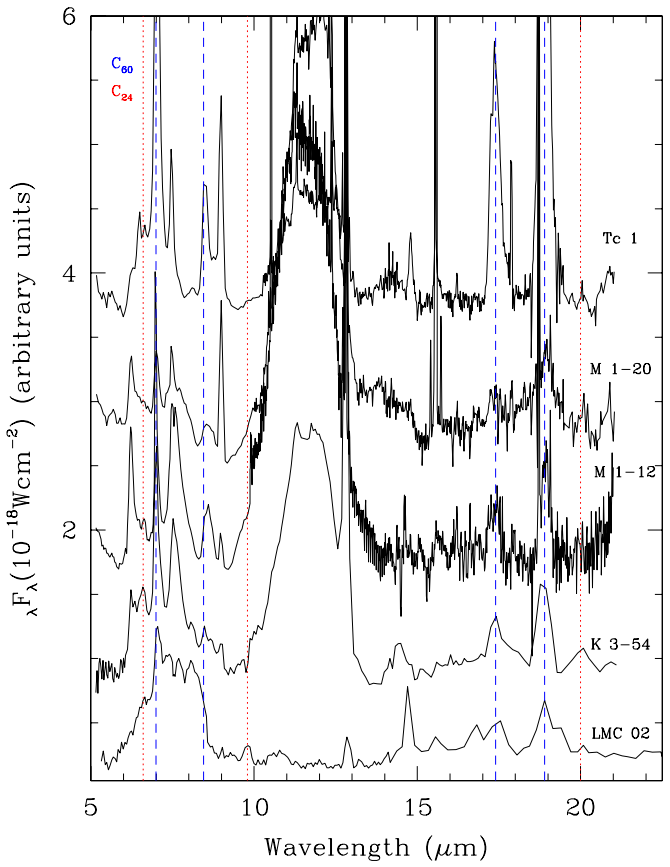

Figure 5. Residual spectra in the wavelength range ∼5–23 μm for four Galactic fullerene PNe (Tc 1, M 1−20, M 1−12, and K 3−54) in comparison with the extragalactic PN LMC 02. The band positions of C_{60} (dashed) and planar C_{24} (dotted) are marked (see the text for more details). Note that the spectra are artificially displaced in the vertical axis for clarity.

(A color version of this figure is available in the online journal.)

are needed in order to reach any firm conclusion about the relative spatial distribution of C_{60}, AIBs, and other emission in Tc 1.

Figure 5 displays the residual spectra of the galactic fullerene PNe Tc 1, M 1−20, M 1−12, and K 3−54 and the extragalactic PN LMC 02. The expected positions of the four C_{60} bands are marked with dashed vertical lines. We would like to remark that two additional MC PNe (SMC 17 and SMC 19; see Stanghellini et al. 2007 for the spectra) show a strong feature at 19.0 μm that could be attributable to C_{60}. However, these PNe show very strong AIBs (e.g., those at 6.2, 7.7, 8.6, and 11.3 μm usually attributed to PAHs) together with a yet unidentified feature at 17.0 μm (see, e.g., Boersma et al. 2010). Given that the other C_{60} features (at ∼7.0 and 17.4 μm) are not obvious in their residual spectra and that the 17.0 and 19.0 μm features may be due to very large PAHs (Boersma et al. 2010), we considered that these two sources do not have solid fullerene detections, and therefore they are not included in the analysis presented here.

For three (Tc 1, LMC 02, and SMC 24) of the C_{60}-containing PNe, high-resolution ($R \sim 600$) *Spitzer*/IRS spectra are also available, in which relatively strong and isolated C_{70} features are present at 12.6, 14.9, 15.6, 17.8, 18.7, and 21.8 μm (von Czarnowski & Meiwes-Broer 1995; see Figure 2 in García-Hernández et al. 2011a). The C_{70} infrared features may be present in PNe other than Tc 1, LMC 02, and SMC 24. Only low-resolution *Spitzer*/IRS spectra were obtained for the MC PNe in our sample, which allowed us to avoid confirming/excluding the detection of these features in more extragalactic sources. However, the Galactic PNe M 1−20, M 1−12, and M 1−60 were observed at high resolution as well and these three PNe show a weak but unblended feature at 21.8 μm (see Figure 2) that we attribute to C_{70}. Consistent with our identification, M 1−60 and M 1−20 also show some C_{70} emission at 14.9 μm (Figure 5). We do not estimate the C_{70} abundances and temperatures in these three sources due to the intrinsic weakness of these possible C_{70} features and because we only see a maximum of two unblended C_{70} features (see Section 3.2).

We report for the first time the presence of unusual IR features at ∼6.6, 9.8, and 20 μm, which are coincident with the strongest transitions of planar C_{24} (graphene precursors or "proto-graphene") in the Galactic PN K 3−54. These features were detected in another two targets that also have fullerenes, LMC 02 and SMC 24 (García-Hernández et al. 2011a). Among the other Galactic fullerene PNe, only M 1−12 displays a strong 6.6 μm feature. Although more tentative, the 6.6 μm feature seems also to be present in Tc 1, M 1−20, and M 1−60 (see Figure 5).

In Table 1, we give the positions and integrated fluxes for the C_{60} and C_{70} fullerene bands identified in the 16 fullerene PNe, as well as the possible planar C_{24} features. These measurements have been done in the residual spectra by fitting a baseline to the local continuum of each infrared band in order to subtract any possible extra contribution from the underlying dust features at 6–9, 9–13, and 15–20 μm (see Figures 2–4) still present in the dust continuum subtracted spectra. We also list in Table 1 our estimated flux errors between brackets, which take into account the error in the measurement as well as the error introduced by the uncertainty of the determination of the local baseline selected for integrating the fluxes. Our estimated flux errors are typically ∼15% for the Galactic PNe and the strongest fullerene transitions (e.g., at 17.4 and 18.9 μm) in the PNe of the MCs. The estimated flux errors are, however, higher for the weaker fullerene transitions (e.g., at 7.0 and 8.5 μm) observed in MC PNe, which sometimes can be as high as ∼30–40% (Table 1). Note also that the observed 7.0 μm emission is a blend of C_{60}, C_{70}, and [Ar II] 6.99 μm emission. We estimate the C_{60} and C_{70} 7.0 μm flux contributions from the corresponding Boltzmann excitation diagrams below (Section 3.2). The position and flux for the 15.6 μm C_{70} band is only given when this feature is not blended with the usually stronger 15.6 μm [Ne III] emission.

Table 2 gives some basic physical parameters available in the literature, such as the effective temperature of the central star, the H_β flux, carbon abundance, electron temperature and density, and total hydrogen and carbon mass of the nebula.

3.1. CLOUDY Photoionizaton Models with Line- and Wind-blanketed Atmospheres

In a previous work, we presented some basic *CLOUDY* models (Ferland et al. 1998) for the fullerene PNe in the MCs (García-Hernández et al. 2011a). We were only interested in doing some general and basic model predictions to explore the possible origins of the 7.0 μm emission and the usually low [Ne III]/[Ne II] ratios observed in fullerene PNe. To do so, we adopted the stellar ionizing continuum blackbodies (BBs) and stellar spectra from Rauch (2003) and concluded that the 7.0 μm emission in fullerene PNe cannot be attributed solely to [Ar II] 6.99 μm but also to a combination of C_{60} and C_{70}. Furthermore, the fact that those models were unable to explain the low [Ne III]/[Ne II] ratios by photoionization, and given

Table 1
Mid-IR C_{60}, C_{70}, and Planar C_{24} Features in Fullerene PNe[a]

Object	λ (μm)	Flux (W cm^{-2})	λ (μm)	Flux (W cm^{-2})	λ (μm)	Flux (W cm^{-2})	λ (μm)	Flux (W cm^{-2})
				C_{60}				
SMC 13	7.13	4.00e-21(±1.00)	8.66	2.53e-21(±0.63)	17.50	7.59e-22(±1.52)	18.98	3.66e-21(±0.55)
SMC 15	7.09	4.01e-21(±1.20)	8.43	1.49e-21(±0.45)	17.49	9.07e-22(±1.81)	18.98	3.03e-21(±0.45)
SMC 16	7.02	6.64e-21(±1.33)	8.57	2.71e-21(±0.81)	17.40	3.78e-21(±0.57)	18.97	8.33e-21(±1.25)
SMC 18	7.03	5.46e-21(±1.37)	8.68	2.66e-21(±0.57)	17.41	2.25e-21(±0.34)	18.96	5.16e-21(±0.77)
SMC 20	7.00	1.57e-21(±0.47)	8.40	4.18e-22(±1.25)	...	...	19.01	3.27e-21(±0.65)
SMC 24	7.04	6.22e-21(±1.24)	8.62	4.07e-21(±1.22)	17.52	4.19e-21(±0.63)	18.94	7.93e-21(±1.19)
SMC 27	7.27	2.65e-21(±1.06)	8.57	1.09e-21(±0.44)	17.34	1.14e-21(±0.34)	18.99	2.29e-21(±0.46)
LMC 02	7.04	7.43e-21(±1.49)	8.58	3.27e-21(±0.98)	17.44	3.31e-21(±0.50)	18.92	4.66e-21(±0.70)
LMC 25	6.92	1.43e-21(±0.36)	8.51	2.26e-21(±0.57)	17.39	6.05e-21(±1.21)	18.97	8.77e-21(±1.32)
LMC 48	7.03	4.47e-21(±1.12)	8.65	2.85e-21(±0.71)	17.45	1.48e-20(±0.30)	18.97	1.31e-20(±0.20)
LMC 99	6.96	3.13e-21(±0.94)	8.70	5.05e-21(±1.01)	17.36	3.81e-21(±0.57)	19.00	5.27e-21(±0.79)
Tc 1	7.02	1.68e-18(±0.25)	8.51	5.96e-19(±0.89)	17.33	8.78e-19(±1.32)	18.89	1.65e-18(±0.25)
M 1−20	7.02	1.04e-19(±0.21)	8.58	6.79e-20(±1.36)	17.35	6.70e-20(±1.01)	18.96	1.36e-19(±0.20)
M 1−12	6.99	2.24e-19(±0.34)	8.58	1.07e-19(±0.16)	17.37	6.48e-20(±0.97)	18.94	1.29e-19(±0.19)
M 1−60	7.00	9.59e-20(±1.92)	8.61	7.13e-20(±1.43)	17.34	3.73e-19(±0.56)	19.15	6.82e-19(±1.02)
K 3−54	7.01	5.79e-20(±0.87)	8.48	3.83e-21(±0.77)	17.38	2.58e-20(±0.39)	18.86	4.06e-20(±0.61)
				C_{70}				
SMC 24	14.93	2.45e-21(±0.73)	15.56	7.49e-21(±1.50)	17.77	2.96e-21(±0.59)	...	...
LMC 02	...	...	15.57	6.37e-22(±1.27)	17.72	1.56e-22(±0.47)	18.73	8.02e-22(±1.60)
Tc 1	12.53	4.24e-20(±0.85)	14.79	8.34e-20(±1.67)	15.55	1.01e-19(±0.20)	21.75	2.71e-20(±0.68)
				C_{24}				
SMC 24	6.62	7.25e-21(±1.45)	9.79	2.20e-21(±0.44)	20.02	5.03e-21(±1.01)	...	...
LMC 02	...	...	9.79	2.66e-21(±0.53)	20.08	9.52e-22(±1.90)	...	...
K 3−54	6.59	1.19e-20(±0.18)	9.60	5.56e-21(±1.12)	20.02	1.14e-20(±0.17)	...	...

Notes. [a] The first 11 PNe pertain to the Magellanic Clouds while the other five objects are located in our own Galaxy. Estimated flux errors (between brackets) are always less than ∼30%–40%. The estimated flux errors are lower (typically ∼ 15%) for the Galactic PNe as well as for the strongest fullerene transitions (e.g., at 17.4 and 18.9 μm) in PNe of the Magellanic Clouds (see the text for more details).

that fast stellar winds from the central stars are ubiquitous in PNe (and the associated shocks), lead us to the suggestion of a possible shock-excited origin for the [Ne II] 12.8 μm emission in fullerene PNe (see García-Hernández et al. 2011a for more details). We did not contemplate the possibility, however, that the observed [Ne III]/[Ne II] ratios also might be explained by using model atmospheres with line (and wind) blanketing (C. Morisset 2011, private communication; see also Morriset et al. 2004 and references therein). Here, we present new radiation transfer modeling exploring this option.

We used version C08.01 of the photoionization code *CLOUDY* to model the nebular emission in our fullerene sources. For the model atmosphere of the central star, we used the grid of models provided by Pauldrach et al. (2001), which are available in *CLOUDY*, identified as tables WMBasic. These models include non-LTE, line- and wind-blanketed model, atmospheres for OB stars with solar and sub-solar metallicities. For all models, we have assumed a constant luminosity of 10^4 $L_{\odot}$ of the star and a fixed distance to the nebula of 0.1 pc (inner radius). Variations of luminosity and/or inner radius closely mimic variations of the temperature of the central star. Thus, our sequences (varying central star temperature) represent the locus of a given model for any combination of luminosity, distance, and temperature. We computed models using solar and sub-solar metallicities for the atmosphere of the central star, but there are no large differences in the resulting line ratios. We assumed for the abundances of the nebula those for the prototype fullerene PN Tc 1 and quoted by Pottasch et al. (2011) in Table 15. We considered a spherical geometry for the nebula with a density of 1800 cm^{-3} at the inner radius, and a dependency with the distance to central ionizing source as r^{-2}. The chemical abundances of the photoionized gas are also those quoted by Pottasch et al. (2011) in their Table 15.

In Figure 6, we display our model predictions compared to the observed line ratios ([Ar II]/H I versus [Ar III]/H I and [S IV]/[S III] versus [Ne III]/[Ne II]) in the fullerene PNe of our sample. In the right panel, we present a combination of line ratios ([S IV]/[S III] versus [Ne III]/[Ne II]), which permits determination of the effective temperature ($T_{\rm eff}$) of the central star, independently of the nebular abundances. It can clearly be seen that model atmospheres with line and wind blanketing can explain many of the observed [Ne III]/[Ne II] ratios. In addition, all fullerene sources show a rather narrow range in effective temperature ($T_{\rm eff}$ ∼ 30,000–45,000 K).

The fact that line and wind blanketing can explain many of the observed [Ne III]/[Ne II] ratios weakens the hypothesis of a shock-excited origin for the [Ne II] 12.8 μm emission. Unfortunately, the shock hypothesis cannot be directly tested with the present data.

It should be noted that the observed central star effective temperatures determinations in the literature (listed in Table 2) came mostly from hydrogen Zanstra analysis, and thus, although more reliable for optically thick PNe, they should always be used as lower limits for optically thin targets (see also Section 4.1). Moreover, none of the temperature determinations available are free from model assumptions. Indeed, from our *CLOUDY* modeling (see Figure 6), we infer effective temperatures higher than the hydrogen Zanstra temperatures (although always lower

Table 2
The Sample of Fullerene PNe

Object	$T_{\rm eff}$ (K)	$\log(F(H_\beta))$	A(C) log(C/H)+12	T_e (10^4 K)	N_e (cm^{-3})	Ref.[a]	M_H ($M_\odot$)	M_C (10^{-3} $M_\odot$)
SMC 13	31,300	−12.59	8.73	1.28	2900	(1,2,3,4,4)	0.702	4.520
SMC 15	...	−12.45	8.26	1.41	7500	(⋯ ,5,3,6,7)	0.270	0.588
SMC 16	...	−12.74	8.19	1.18	4400	(⋯ ,5,3,6,7)	0.210	0.392
SMC 18	...	−12.66	8.31	1.18	3600	(⋯ ,2,3,4,4)	0.381	0.934
SMC 20	...	−12.47	8.25	1.38	3900	(⋯ ,2,3,4,4)	0.497	1.061
SMC 24[b]	37,800	−12.66	8.18	1.16	2800	(1,2,3,4,4)	0.411	0.747
SMC 27	43,300	−12.51	...	1.27	3650	(1,2, ⋯ ,4,4)	0.471	...
LMC 02[b]	39,000	−13.18	8.14	1.21	5000	(8,7,9,6,8)	0.048	0.079
LMC 25	33,700	−12.39	8.29	1.56	3300	(10,11,12,13,13)	0.626	1.465
LMC 48	...	−12.48	8.40	1.00[c]	1900	(⋯ ,5,12, ⋯ ,6)	0.844	2.540
LMC 99	...	−12.54	8.77	1.22	3600	(⋯ ,14,15,6,6)	0.434	3.040
Tc 1[b]	34,100	−10.73	8.67	0.90	3000	(16,17,18,18,18)	0.0535	0.300
M 1−20[d]	53,000	−11.93	8.55	1.11	7500	(19,17, ⋯ ,20,21)	0.1558	0.715
M 1−12[d]	29,100	−11.60	8.82	0.95	7400	(16,17, ⋯ ,22,23)	0.1708	1.354
M 1−60[d]	74,400	−12.28	8.82	0.92[e]	9200[e]	(16,17, ⋯ ,24,24)	0.1752	1.384
K 3−54[d]	...	−13.30	8.55	1.02	5000[f]	(⋯ ,25, ⋯ ,17, ⋯)	0.0619	0.263

Notes.
[a] References for $T_{\rm eff}$, $\log(F(H_\beta))$, C abundance, T_e, and N_e. Note that literature $T_{\rm eff}$ values are mostly H I Zanstra temperatures (see Section 3.1).
[b] T_e for LMC 48 is assumed to be 10^4 K.
[c] High-resolution *Spitzer*/IRS spectra were obtained and it was possible to detect C_{70} unambiguously.
[d] The C abundance for these PNe is assumed from the average values of the height above the Galactic plane (see the text).
[e] T_e and N_e for M 1−60 are derived by using the line fluxes given by Girard et al. (2007).
[f] N_e for K 3−54 is assumed to be 5000 cm^{-3}.
References. (1) Villaver et al. 2004; (2) Stanghellini et al. 2003; (3) Stanghellini et al. 2009; (4) Shaw et al. 2010; (5) Shaw et al. 2006; (6) Leisy & Dennefeld 2006; (7) Dopita et al. 1988; (8) Herald & Bianchi 2004; (9) Milanova & Kholtygin 2009; (10) Villaver et al. 2003; (11). Stanghellini et al. 2002; (12) Stanghellini et al. 2005; (13) R. A. Shaw et al. (2013, in preparation); (14) R. A. Shaw (2011, private communication); (15) Leisy & Dennefeld 1996; (16) Preite-Martínez et al. 1989; (17) Cahn et al. 1992; (18) Pottasch et al. 2011; (19) Kaler & Jacoby 1991; (20) Chiappini et al. 2009; (21) Richer et al. 2008; (22) Henry et al. 2010; (23) Stanghellini & Kaler 1989; (24) Girard et al. 2007; (25) Acker et al. 1991.

than 45,000 K) for all of these MC PNe. The only exception is LMC 02 for which the [S IV]/[S III] ratio is somewhat lower than expected for its $T_{\rm eff}$ (39,000 K as derived from *FUSE* data; we attribute this difference to a contamination by C_{70} of the observed 18.7 μm emission. From Figure 6, it is also evident that for Galactic PNe M 1−20 and M 1−60 the models indicate $T_{\rm eff} \sim$ 40,000–45,000 K,[14] whereas for Tc 1 $T_{\rm eff} \simeq$ 35,000 K. Note that the Galactic PNe M 1−12 and K 3−54 are not shown in this diagram because they only present [Ne II] 12.8 μm and [S IV] 10.5 μm emission, respectively. An anomalous high value of [Ne II] 12.8 μm emission (e.g., as a consequence of strong shocks) in these sources cannot be discarded.

In the left panel of Figure 6 ([Ar II]/H I versus [Ar III]/H I), we illustrate how varying the abundance of Ar noticeably affects the line ratios involving these lines. It can be seen that the observed values of [Ar III]/H I can be explained with the model effective temperature, consistent with the values derived from the [S IV]/[S III] versus [Ne III]/[Ne II] diagram shown in the right panel of Figure 6. However, none of the models can explain (even taking into account maximum errors of 40% in the observed line intensity ratios) the high observed values of the [Ar II]6.99 μm/H I line flux ratio. For example, in the case of Tc 1 and M 1−12, the expected ratios are around 1, whereas in the case of M 1−20 and M 1−60 those are around 0.1. Note that PN K 3−54 does not appear in this diagram because the H I 7.5 μm line is blended with the much stronger 7.7 μm AIB. Thus, the new *CLOUDY* modeling confirms that the 7.0 μm emission in fullerene PNe cannot be attributed uniquely to [Ar II] 6.99 μm, and the C_{60} and C_{70} emission contributions have to be taken into account.

3.2. Boltzmann Excitation Diagrams of the Fullerene Emission

Our previous work indicates that the fullerene emission in PNe of the MCs likely originates from solid-phase fullerene molecules, which are formed on the surface of pre-existing VSGs (or HACs) (García-Hernández et al. 2011a; Duley & Hu 2012). This conclusion was based on the fact that the observed C_{60} 7.0/18.9, 8.5/18.9, and 17.4/18.9 intensity ratios differ from the theoretical predictions for UV-excited gas-phase C_{60} molecules given by Sellgren et al. (2010). Here, we determined the fluxes of the 7 and 8.5 μm C_{60} transitions (which are actually only due to C_{60}) in the Galactic PNe M 1−20, M 1−12, M 1−60, and K 3−54[15] and we constructed the corresponding Boltzmann excitation diagrams (see below for more details) for these Galactic PNe.

In Table 3, we list the C_{60} intensity ratios in fullerene PNe of our Galaxy in comparison with the values derived for fullerene PNe in the MCs. Note that the listed C_{60} $F(7.0)/F(18.9)$ flux ratios are obtained by correcting the observed emission

[14] The *CLOUDY* $T_{\rm eff}$ for M 1−20 and M 1−60 are significantly lower than the literature values (Table 2) and derived from the Zanstra H I method in M 1−20 (Kaler & Jacoby 1991) and the Energy-Balance method in M 1−60 (Preite-Martínez et al. 1989).

[15] Note that the observed 8.5 μm fluxes cannot be completely explained by C_{60} emission in a few MC PNe (SMC 13, 24, LMC 02, 99; see García-Hernández et al. 2011a) and in two Galactic PNe (K 3−54 and M 1−12) only. Thus, these objects may show some AIB emission (e.g., from PAHs) at this wavelength.

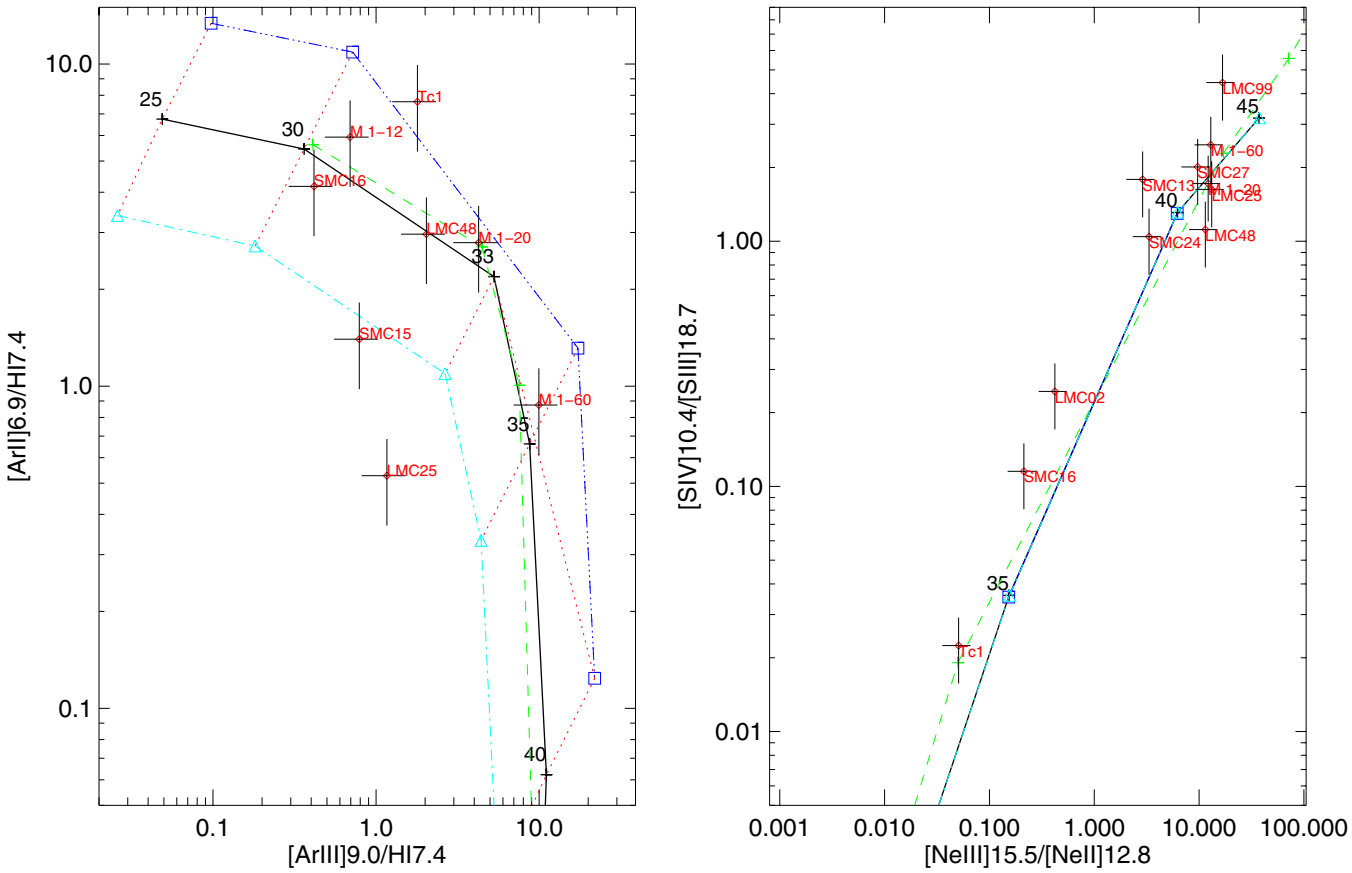

Figure 6. Comparison of *CLOUDY* photoionization models with observed line ratios in fullerene PNe. The black continuous line represents the WMBasic model described in the text, using solar metallicity for the star atmosphere. The model represented with the green line corresponds to a sub-solar metallicity. The number close to each point indicates the value of central star temperature in units of 10^3 K. The models in the left panel displayed by dot-dashed (cyan) and dot-dot-dashed (blue) lines represent models with Ar abundance a factor of two below and above those quoted by Pottasch et al. (2011), respectively. The dotted lines join models with the same value of the star temperature. Error bars of 40% in the observed line intensity ratios are also shown.

(A color version of this figure is available in the online journal.)

Table 3
C_{60} Intensity Ratios and Fullerene Abundances and Temperatures

Object	$F(7.0)/F(18.9)$[a]	$F(8.5)/F(18.9)$[a]	$F(17.4)/F(18.9)$[a]	[Ne III]/[Ne II]	C_{60}/C (%)	f_{C60}[b] (%)	T_{C60} (K)	C_{70}/C (%)	f_{C70}[b] (%)	T_{C70} (K)	C_{70}/C_{60}
SMC 13	0.16	0.32	0.21	2.89	0.003	15 ± 10	453 ± 50	...	...	...	...
SMC 15	0.20	0.49	0.30	0.49	0.07	15 ± 10	290 ± 20	...	...	...	...
SMC 16	0.24	0.33	0.45	0.21	0.12	30 ± 10	414 ± 50	...	...	...	...
SMC 18	0.16	0.52	0.44	1.16	0.03	15 ± 10	365 ± 35	...	...	...	...
SMC 20	0.05	0.13	...	0.41	0.03	10 ± 10	228 ± 30	...	...	...	...
SMC 24	0.47	0.18	0.53	3.33	0.07	60 ± 20	514 ± 30	0.001	20 ± 10	383 ± 60	0.02
SMC 27	0.58	0.48	0.50	9.69	...	50 ± 10	553 ± 40	...	...	...	...
LMC 02	0.48	0.37	0.71	0.42	0.29	30 ± 10	502 ± 20	0.07	10 ± 10	324 ± 10	0.21
LMC 25	0.08	0.26	0.69	13.19	0.02	50 ± 20	300 ± 25	...	...	...	...
LMC 48	0.07	0.22	1.13	11.46	0.01	20 ± 10	270 ± 20	...	...	...	...
LMC 99	0.30	0.56	0.72	16.82	0.02	50 ± 10	446 ± 25	...	...	...	...
Tc 1	0.26	0.36	0.53	0.05	0.04	25 ± 10	415 ± 30	0.005	40 ± 10	314 ± 30	0.10
M 1−20	0.38	0.50	0.49	12.22	0.02	50 ± 10	480 ± 50	...	...	...	...
M 1−12	0.78	0.58	0.50	...	0.02	45 ± 15	660 ± 100	...	...	...	...
M 1−60	0.04	0.11	0.55	12.94	0.05	30 ± 10	260 ± 30	...	...	...	...
K 3−54	0.29	0.25	0.64	0.02	0.01	20 ± 10	360 ± 50	...	...	...	...

Notes.

[a] The ratio of fluxes in the C_{60} bands with the wavelengths in brackets. Note that we list the C_{60} intensity ratios obtained by correcting the observed emission fluxes at 7 μm (also at 8.5 μm for some PNe in our sample) by the C_{60} contribution factors (f_{C60}) derived from the Boltzmann excitation diagrams (see the text for more details).

[b] C_{60} and C_{70} contributions to the observed 7 μm flux.

fluxes at 7 μm by the C_{60} contribution factors (f_{C60}) derived from the Boltzmann excitation diagrams (see below) and also listed in Table 3. In addition, the listed C_{60} $F(8.5)/F(18.9)$ intensity ratios in a few sample PNe (see above) were corrected by their corresponding contribution factors at 8.5 μm (not shown in Table 3). From the results obtained, we can reach a similar conclusion about the fullerene excitation mechanism for the subsample of fullerene-detected PNe in our Galaxy (see Table 3). In particular, the C_{60} 7.0/18.9 and 8.5/18.9 ratios indicate photon energies of less than 5 eV, regardless of the central star temperatures (between ~30,000 K and 45,000 K). In addition, the C_{60} 17.4/18.9 intensity ratio strongly varies from source to source (from 0.21 to 1.13), while this ratio is predicted to be insensitive to the energy of the absorbed UV photons (a C_{60} 17.4/18.9 ratio of 0.28–0.38 is predicted by Sellgren et al. 2010) for gas-phase fullerene molecules. It should be noted that our conclusion is different from that very recently drawn by Bernard-Salas et al. (2012). However, the other fullerene C_{70} also contributes to the observed 7 μm flux (Iglesias-Groth et al. 2011; García-Hernández et al. 2011a)—e.g., in Tc 1, the C_{70} flux contribution (40%) is even higher than that for C_{60} (25%). Our conclusion is supported by the fact that the same temperatures (within the errors) are needed to explain both the 7.0 and 8.5 μm C_{60} band strengths. Finally, we note that taking into account the uncertainties of flux measurements and Einstein coefficients, our average intensity $C_{60}F(7.0)/F(18.9)$ (=0.28), $F(8.5)/F(18.9)$ (=0.35), and $F(17.4)/F(18.9)$ (=0.56) ratios would be more consistent with the C_{60} intrinsic strengths reported by Fabian (1996) and Iglesias-Groth et al. (2011). Thus, in the following, we will assume that the fullerene emission in PNe is originated from solid-state fullerenes.

We can determine the fullerene excitation temperature for each PN from the flux measurements of the C_{60} and C_{70} transitions (see Table 1) and the absorptivity measurements recently obtained by Iglesias-Groth et al. (2011). Absorptivity for each transition led to an *f*-value from which the Einstein coefficient A_{ij}, is derived which provides a relation between the emitted flux and the number of molecules populating the energy level associated with the transition (see, e.g., Cami et al. 2010 for more details).

We adopted the temperature dependence of the absorptivity for each C_{60} and C_{70} transition given in Iglesias-Groth et al. (2011) and developed an iterative process to find the best possible correlation coefficient in the plane $\ln(N_u/g_u)$ versus E_u/k independently for each fullerene. A thermal distribution over the excited states will be indicated by collinear data points in the Boltzmann excitation diagram. In this case, the slope and the intercept of the linear relation determines the temperature and total number of emitting fullerene molecules. The initial temperatures for this iterative process were assumed in the range from 100 to 1000 K and only a few iterations were required for a quick convergence. The temperature values for C_{60} and C_{70} derived this way are listed in Table 3. The four mid-IR transitions of C_{60} were considered, allowing the fraction of the flux of the 7 μm transition—which is actually due to C_{60}—to be a free parameter because of the possible contamination with C_{70} and the [Ar II] nebular line. The best linear fit is sensitive to this fraction, and thus we also iterated on this parameter in order to explore the full range of possible values (from 0 to 1). In the case of C_{70}, we considered the three or four (depending on the source and the signal-to-noise ratio (S/N) of the spectrum; see Table 1 for the C_{70} features used for each source) mid-infrared transitions less contaminated by other species, iterating also on the fraction of the 7 μm flux that may be due to C_{70}. We generally found very good correlation coefficients that are always higher than 0.89. Figure 7 illustrates examples of the Boltzmann excitation diagrams for the C_{60} (left panel) and C_{70} (right panel) fullerene emission detected in the MC PNe SMC 16 and LMC 02, respectively.

The fullerene PNe in the MCs were previously studied by us in García-Hernández et al. (2011a). The sources in the MCs offer a more reliable estimation of the C_{60} and C_{70} abundances in PNe than in their Galactic counterparts. This is because the distances to the MCs (48.5 and 61 kpc for the LMC and SMC, respectively) are accurately known and reliable C abundances are also available in the literature (García-Hernández et al. 2011a). However, this is not the case for the five fullerene PNe in our Galaxy—in addition, only Tc 1 has a reliable C abundance in the literature (Table 2). For consistency, we decided to assume the recent statistical distances by Stanghellini & Haywood (2010) for four of the Galactic sources: M 1−20 (8.0 kpc), M 1−12 (9.2 kpc), M 1−60 (9.5 kpc), and K 3−54 (23.4 kpc). The only exception is Tc 1[16], for which we assumed a distance of 2 kpc for comparison with Cami et al. (2010). Following Milanova & Kholtygin (2009), we may assign a PN type (i.e., type I, IIa, IIb, III, and IV)[17] and an average carbon abundance ($A(C) = \log(C/H)+12$) to each Galactic PN from the height above the Galactic plane z. Therefore, we assume a type IIa and $A(C) = 8.55$ for M 1−20 ($z = 0.492$ kpc) and K 3−54 ($z = 0.547$ kpc) as well as a type IIb and $A(C) = 8.83$ for M 1−12 ($z = 0.258$ kpc) and M 1−60 ($z = 0.290$ kpc). The IIab PN types of the Galactic fullerene PNe, as derived by this very rough and limited method, seem to be consistent with that of Tc 1, which is identified as a slowly evolving low-mass type II PN (García-Hernández et al. 2010). In addition, as we will see in Section 4.1, all fullerene PNe are likely of low mass and are slowly evolving toward the white dwarf stage. Table 2 lists all relevant information (e.g., H_β flux, C abundance, electron temperature and density, and total hydrogen and carbon masses of the nebula) as well as the source of information used in each case from the literature for all fullerene PNe in our sample.

By using the above distances, the number of C_{60} and C_{70} molecules (or masses of pure C_{60} and C_{70}) was estimated for all sources in our sample, and the C_{60}/C and C_{70}/C abundances listed in Table 3 were derived from the total carbon and hydrogen mass of the nebula. The total H mass of the nebula is obtained from the electronic temperature and density and the observed H_β flux, while the total carbon mass is obtained from the total H mass and C abundance of the nebula. The corresponding C_{70}/C_{60} ratios are also given in Table 3. We find C_{60}/C ~0.01%–0.05% (average of 0.03%) and $T_{C60} = 260$–660 K for the four Galactic fullerene PNe studied for the first time in this paper. The formal error of our fullerene abundance estimations are difficult to evaluate because we used different literature sources for the C abundance, electron density, etc. However, it should be noted that by giving the C_{60}/C and C_{70}/C abundance ratios, the distance dependence is canceled. Thus, the main sources of error are the electronic density and carbon abundance. We estimate that the errors of our fullerene abundances in MC PNe are certainly lower than 50% (likely much lower for most of

[16] Stanghellini & Haywood (2010) give a statistical distance of 2.7 kpc toward Tc 1.

[17] For type I ($|z| = 0.23$ kpc) $A(C) = 8.32$, for type IIa ($|z| = 0.31$) $A(C) = 8.82$, for type IIb ($|z| = 0.56$) $A(C) = 8.55$, for type III ($|z| = 1.05$) $A(C) = 8.60$, and for type IV ($|z| = 1.35$) $A(C) = 8.64$ (see Table 5 in Milanova & Kholtygin 2009).

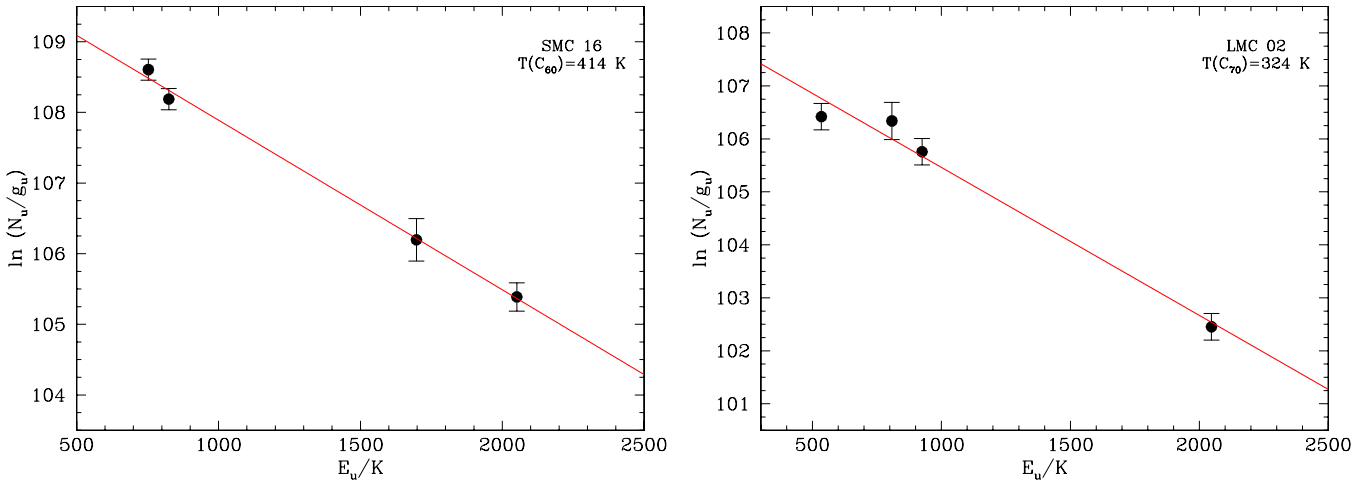

Figure 7. Illustrative examples of the Boltzmann excitation diagrams ($\ln(N_{nu}/g_u)$ vs. E_u/k) obtained for the C_{60} and C_{70} bands observed in the PNe SMC 16 (left panel) and LMC 02 (right panel), respectively (see the text).

(A color version of this figure is available in the online journal.)

the MC PNe sample), but the maximum error in the C_{60}/C ratio for the Galactic PNe (with the exception of Tc 1 for which the C abundance is more accurately known) may be a factor two or three. Taking into account all assumptions made regarding the Galactic objects, our individual and average C_{60}/C abundances as well as the C_{60} temperatures for these sources are very similar to the C_{60} abundances obtained in the MCs (see Table 3). Finally, note that we estimate $C_{60}/C = 0.04\%$ and $C_{70}/C = 0.005\%$ in Tc 1, which are a factor of 40 and 300, respectively, lower than the ∼1.5% estimates for both species by Cami et al. (2010).

4. DISCUSSION

4.1. Evolutionary Status of the Fullerene PNe

The temperature and luminosity of central stars of PNe are important parameters in order to determine the evolutionary status of the nebula. Central star temperatures are available for a sizable number of objects in the sample of PNe with fullerenes (nine PNe). However, most of the temperature determinations of the objects at hand rely on widely used indirect methods: either Zanstra (Zanstra 1931) or the Energy Balance (Stoy 1933), with only one exception, LMC 02, obtained from *FUSE* data (Herald & Bianchi 2004). Moreover, for those PNe for which Zanstra temperatures have been obtained (SMC 13, SMC 24, SMC 27, and LMC 25), only hydrogen Zanstra temperatures could be determined, for which the optically thick nature of the nebulae to all the photons above the Lyman limit of H is not assured. An indication that the effective temperature of these stars cannot be much higher than ≈50,000 K is provided by the lack of detection of He II 4686 Å nebular line flux and confirmed by our new *CLOUDY* modeling (see Section 3.1).

Although not definitive, conclusions can be drawn given the small number of objects and the uncertainties; the available data show that all the PNe with fullerenes have central stars with low effective temperatures in the range between ∼30,000 and 45,000 K. Given the paths that these stars follow in the H-R diagram, a low temperature can imply a very old or a very young star, therefore a second parameter, stellar luminosity (or mass), is needed in order to understand their evolutionary status. Unfortunately, central star luminosity determinations rely on the availability of the distances accurately determined for a handful of objects in the Galaxy and none of the fullerene-containing PNe are among them. The situation is quite different for the PNe located at the known distances of the MCs. In this case, determinations of the central star luminosities are possible with great accuracy provided that the central star flux is measured. Out of the 11 PNe in the clouds, only 3 of them have measured luminosities (see Villaver et al. 2003, 2004); the reasons are either the objects were not observed with the appropriate instrumentation in order to measure the stellar flux (six PNe), the star was saturated (LMC 25), or the central star was below the nebular level and thus not detected (SMC 13).

PNe SMC 24, SMC 27, and LMC 02 are the only ones that we can analyze in full given that they have both luminosities and effective temperatures available (Villaver et al. 2004; Herald & Bianchi 2004). Although conclusions from three objects cannot be extrapolated to the full sample, we find it meaningful that these three have luminosities that locate them in the horizontal part of the post-AGB tracks for central stars of PNe. Together with their low effective temperatures, this indicates that at least these three objects are truly unevolved stars for which less than ≈10,000 yr (central star time according to Vassiliadis & Wood 1994) could have passed since the moment the star left the AGB phase. Moreover, all three objects have central stars in the low-mass range: 0.59 $M_\odot$ for SMC 24, 0.60 $M_\odot$ for SMC 27, and 0.56 $M_\odot$ for LMC 02, implying that the three of them descend from a low-mass progenitor with a main-sequence mass $<1.5\ M_\odot$. It is important to note that the masses of fullerene systems in the SMC are within the average mass of central stars of PNe in the SMC, 0.63 $M_\odot$ (Villaver et al. 2004), while the LMC object is significantly less massive than the average (0.65 $M_\odot$ central star mass) (Villaver et al. 2003, 2007).

The central star and nebular gas are interdependent systems, that is, the evolution of the nebulae is governed by the energetics provided by the central star mostly through the stellar wind and ionizing radiation field. In that sense, the physical radius of the PNe can provide an indirect way of evaluating the evolutionary status of the systems provided that for the objects in the MCs this quantity is available. If we take the photometric radius of the nebulae[18] from *Hubble Space Telescope* (*HST*) data in

[18] The photometric radius, $R_{\rm phot}$, corresponds to the size of a circular aperture that contains 85% of the flux in [O III] λ5007. $R_{\rm phot}$ gives an objective measurement of the nebular angular size that is insensitive to the S/N ratio of the image and is useful for evolutionary studies.

Stanghellini et al. (2003) and Shaw et al. (2006) and then adopt a distance to the SMC of 61 kpc and to the LMC of 48.5 kpc, we obtain the physical radius of the PNe in the MCs. With only one exception, LMC 99 (with a physical radius of 0.1 pc), all the radii are <0.06 pc. The average radius of all the PNe in the MCs that contain fullerenes is 0.058 pc (or 0.054 pc if we exclude LMC 99). The majority of the PNe in the *HST* samples have small sizes; they were selected to avoid entangled lines in the STIS spectroscopic observations. They have a median photometric radius of 0.10 pc in the LMC and 0.08 pc in the SMC (see Shaw et al. 2006). The samples of MC PNe that contain fullerenes have physical sizes even smaller (most of them <0.06 pc) than the average values. Irrespective of the mechanism, whether at the expense of the energy provided by the hot bubble (the high-velocity wind producing an adiabatic shock) or by the propagation of the ionization front, shell growth is expected to increase with time (see Villaver et al. 2002b). Thus, if we accept physical size as an indicator of the evolutionary status of the nebulae, then the fullerene PNe in the MCs seem to be young (non-evolved) systems, as suggested by their small physical radii that are smaller than the average value of a full sample.

4.2. Fullerene Detection versus Metallicity

Interestingly, the fraction of fullerene-detected PNe increases with decreasing metallicity (∼5% in the Galactic disk versus ∼31% in the MCs). This fraction goes from ∼5% in the Galactic disk (two detections from 39 C-rich compact (<4″) and young PNe; Stanghellini et al. 2012) to ∼20% in the LMC (four detections from 20 C-rich LMC PNe) and ∼44% in the SMC (seven detections from 16 C-rich SMC PNe). In addition, the *Spitzer*/IRS spectra reveal that dust processing is very limited in the low-metallicity environments of the MCs. The size of the dust grains remains small (e.g., Stanghellini et al. 2012) and the formation of PAHs (as indicated by the presence of AIBs) is more difficult at low metallicities (Stanghellini et al. 2007). This indicates that the dust grains are less processed in low-metallicity PNe than in their Galactic counterparts, likely because of the probability of forming big carbon dust aggregates around the central star, which may be affected by the posterior PN evolution—i.e., the quickly changing UV radiation field and/or the post-AGB shocks from the strong stellar winds. This probability decreases with decreasing metallicity.

Although we find meaningful that the fraction of fullerene PNe probably depends upon the metallicity of the host environment, it is worth noting here that selection effects in the *Spitzer* PN samples may play a potentially significant role in the statistics mentioned above. None of these MC PN samples are complete, though the surface brightness was high enough to be included in an *HST* or *Spitzer* sample. However, our estimation of the detection rate of fullerenes (∼5%) in our own Galaxy comes from the sample of 157 compact and young PNe in the Galactic disk (Stanghellini et al. 2012). This Galactic fullerene detection rate may be considered as an upper limit for environments of roughly similar solar metallicity. This is because Stanghellini et al.'s (2012) PNe sample is sampling the early stages of PN evolution and dust processing (see below), when the detection rate of fullerenes is expected to be maximized; the fullerenes are not too cold (e.g., $T_{C60,C70} < 100$ K) to escape detection at mid-infrared wavelengths.

In short, the high detection rate of fullerenes in MC PNe seems to be strongly linked to the limited dust processing (or the general presence of small dust grains) in low-metallicity circumstellar envelopes. This is consistent with the observational finding that the still unidentified 21 μm feature (Kwok et al. 2001; see also García-Hernández 2012 for a recent review) is much more common in post-AGB stars of the MCs than in our own Galaxy (Volk et al. 2011). This suggests that the 21 μm feature is possibly also related with the formation of fullerenes and its carrier may be a fragile intermediate product from the decomposition of HAC or a similar material (see below).

4.3. Broad 6–9, 9–13, 15–20, and 25–35 μm Emission

As we have mentioned before, dust processing seems to depend on metallicity. For example, MC PNe display infrared spectra, which are similar to many Galactic post-AGB stars, where dust evolution is still in its early stages, and/or still taking place. However, in galactic post-AGB stars, we already can see huge 25–35 μm features (e.g., Hrivnak et al. 2000) and very little 6–9, 9–13, and 15–20 μm features, contrary to what we observe in the MCs. It seems that it is now well established that the carrier of unidentified infrared emission (UIE)—both discrete and broad features—observed from ∼3 to 20 μm in C-rich evolved stars should be carbon nanoparticles with mixed aliphatic and aromatic structures similar to that of HAC dust (Kwok et al. 2001; Kwok & Zhang 2011). Note that instead of HAC nanoparticles, other organic matter with a complex mix of aliphatic and aromatic structures (e.g., coal, petroleum fractions, quenched carbonaceous compounds, etc.) may be present in the circumstellar envelopes of evolved stars and might be responsible for the UIE (e.g., Kwok et al. 2001). For example, coal and petroleum fractions may explain a diverse set of aromatic and aliphatic features seen in proto-PNe (e.g., Cataldo et al. 2002). In this context, our *Spitzer* spectra of fullerene PNe also show that a complex mixture of aliphatic and aromatic species (e.g., HACs, PAH clusters, fullerenes, and small dehydrogenated carbon clusters) is present in their circumstellar envelopes.

Our interpretation is that the broad infrared features at 6–9, 9–13, 15–20, and 25–35 μm are intimately related with the formation of fullerenes in PNe, being likely produced by a carbonaceous compound with a mixture of aromatic and aliphatic structures (e.g., HAC) and/or their decomposition products (e.g., fullerene precursors or intermediate products). It should be noted that Kwok et al. (2001) were the first to suggest that the broad 6–9 and 9–13 μm features seen in proto-PNe may be due to a carbonaceous compound with a mixed aromatic/aliphatic structure. The 6–9 and 15–20 μm features, which are almost exclusively seen in low-metallicity MC PNe (Figures 3 and 4), may be due to small dust grains (e.g., HAC nanoparticles), while the 9–13 and 25–35 μm that are seen in all metallicity environments (Figures 2–4) would be produced by big dust grains (e.g., HAC aggregates). The broad 6–9 μm feature may be due to HACs, PAH clusters, or VSGs (see, e.g., Tielens 2008), while the 15–20 μm emission may be identified with the C–C–C bending modes of relatively large PAHs or PAH clusters (Van Kerckhoven et al. 2000). On the other hand, although the broad 9–13 and 25–35 μm features are usually attributed to SiC (the so-called 11.5 μm feature; e.g., Speck et al. 2009) and MgS (e.g., Hony et al. 2002), respectively, these features may be due to bigger dust grains (e.g., HAC aggregates). García-Hernández (2012) argued against the SiC and MgS identification of these features in fullerene PNe and it will not be repeated here. Basically, the 25–35 μm feature may be explained by HACs (see Grishko et al. 2001; García-Hernández et al. 2010), and the spectral characteristics (position

Table 4
Broad 9–13 and 15–20 μm Emission and 6.2, 7.7, and 11.3 μm AIBs in Fullerene PNe[a]

Object	λ (μm)	Flux (W cm^{-2})	λ (μm)	Flux (W cm^{-2})	λ (μm)	Flux (W cm^{-2})	λ (μm)	Flux (W cm^{-2})	λ (μm)	Flux (W cm^{-2})
SMC 13	11.35	4.78e-20(±0.72)	19.06	1.87e-20(±0.28)	6.25	3.74e-21(±0.94)	7.80	8.47e-21(±2.12)	11.23	4.86e-21(±1.22)
SMC 15	11.24	2.51e-19(±0.38)	18.29	1.01e-19(±0.15)	6.21	2.92e-21(±0.88)	7.71	1.17e-20(±0.29)	11.34	3.52e-21(±0.88)
SMC 16	11.56	2.50e-20(±0.38)	...	...	...	...	...	...	11.31	6.75e-23(±2.70)
SMC 18	11.20	1.63e-19(±0.24)	18.53	1.56e-19(±0.23)	...	...	7.74	4.42e-21(±1.33)	11.26	3.85e-21(±1.15)
SMC 20	10.94	2.68e-19(±0.40)	18.05	3.71e-20(±0.56)	6.27	4.21e-21(±1.05)	7.92	4.72e-21(±1.42)	11.33	3.42e-21(±1.03)
SMC 24	11.34	3.85e-20(±0.58)	...	...	6.21	5.36e-22(±2.14)	7.71	3.67e-21(±1.65)	11.30	9.24e-22(±2.31)
SMC 27	11.56	3.09e-20(±0.46)	...	...	...	...	...	...	11.28	2.03e-21(±0.41)
LMC 02	...	...	...	...	6.17	1.71e-22(±0.69)	7.67	4.55e-22(±1.59)	11.29	3.86e-22(±1.55)
LMC 25	11.38	1.74e-19(±0.26)	18.36	1.20e-19(±0.18)	6.28	1.73e-20(±0.26)	7.67	2.95e-20(±0.59)	11.28	4.23e-21(±0.85)
LMC 48	11.41	1.37e-19(±0.21)	17.96	1.25e-19(±0.19)	6.25	9.87e-21(±1.48)	7.55	1.90e-20(±0.38)	11.31	3.26e-21(±0.65)
LMC 99	...	...	...	...	6.27	1.46e-20(±0.22)	7.87	2.68e-20(±0.40)	11.30	1.44e-20(±0.22)
Tc 1	11.75	2.92e-18(±0.44)	...	...	6.22	6.09e-20(±1.22)	...	...	11.28	1.05e-19(±0.16)
M 1−20	11.69	5.20e-18(±0.78)	...	...	6.25	2.01e-19(±0.30)	7.58	2.63e-19(±0.39)	11.29	8.93e-20(±1.34)
M 1−12	11.46	6.53e-18(±0.98)	...	...	6.23	2.32e-19(±0.35)	7.57	4.49e-19(±0.67)	11.26	8.83e-20(±1.32)
M 1−60	11.28	2.91e-18(±0.44)	...	...	6.26	3.08e-19(±0.46)	7.83	1.89e-19(±0.28)	11.30	3.37e-19(±0.51)
K 3−54	11.62	6.94e-19(±1.04)	...	...	6.27	3.46e-20(±0.69)	7.58	5.95e-20(±0.89)	11.29	1.24e-20(±0.19)

Notes. [a] Estimated flux errors (between brackets) are always less than ∼30%–40%. The estimated flux errors are lower (typically ∼15%) for the Galactic PNe as well as for the broad features in Magellanic Cloud PNe.

and shape; see also Table 4) of the 9–13 μm emission differ from those of the SiC 11.5 μm feature.

4.4. Fullerene Emission versus Other IR Features

In this section, we study the fullerene emission in our sample of fullerene PNe versus other solid-state/molecular infrared features. The flux emitted in the C_{60} 18.9 μm feature is roughly correlated with the fullerene content (or C_{60}/C abundance values in Table 3; see also Figure 8) and can be taken as representative of the fullerene emission. Almost all fullerene PNe in our sample show some emission in the broad 9–13 μm feature[19] and in the 11.3 μm PAH feature. However, not all PNe in our sample display evident AIB emissions at ∼6.2 and 7.7 μm or in the very broad 6–9 and 25–35 μm features, which complicates the exploration of any possible relation between the fullerene emission, the carriers of the latter emission features. In particular, we prefer to exclude (on a quantitative basis; see below) the very broad 6–9 and 25–35 μm features from our study. This is because very few fullerene PNe display the 6–9 μm emission, the sensitivity of Infrared Spectrograph (IRS) drops dramatically for $\lambda \geqslant 36$ μm, and previous *Infrared Space Observatory* observations of PNe show that the 25–35 μm feature may go up to wavelengths longer than 40 μm (Hony et al. 2002). The central wavelengths and integrated fluxes of the AIBs (usually attributed to PAHs) at ∼6.2, 7.7, and 11.3 μm, as well as the broad 9–13 and 15–20 μm features, are given in Table 4.

Figure 8 displays the flux ratio C_{60} 18.9 μm/9–13 μm versus the fullerene abundances (in percentage), where we include the propagated error bars corresponding to an individual flux error estimation of ∼15%. Note that we do not include the error bars of the fullerene abundances in order to avoid dulling Figure 8. The formal error in our estimation of the fullerene abundances is difficult to calculate (e.g., there are different literature sources for the C abundance, electron density, etc.), but it should be lower than 50% in the MC sources and likely higher in the Galactic PNe (see Section 3.2). Although most of the sources are concentrated in the lower left corner of the diagram displayed in Figure 8, we find that the flux ratio C_{60} 18.9 μm/9–13 μm seems tentatively to increase with increasing fullerene abundances. Also, two apparent outliers in Figure 8 seem to be PNe Tc 1 and SMC 15. If real, the position of Tc 1

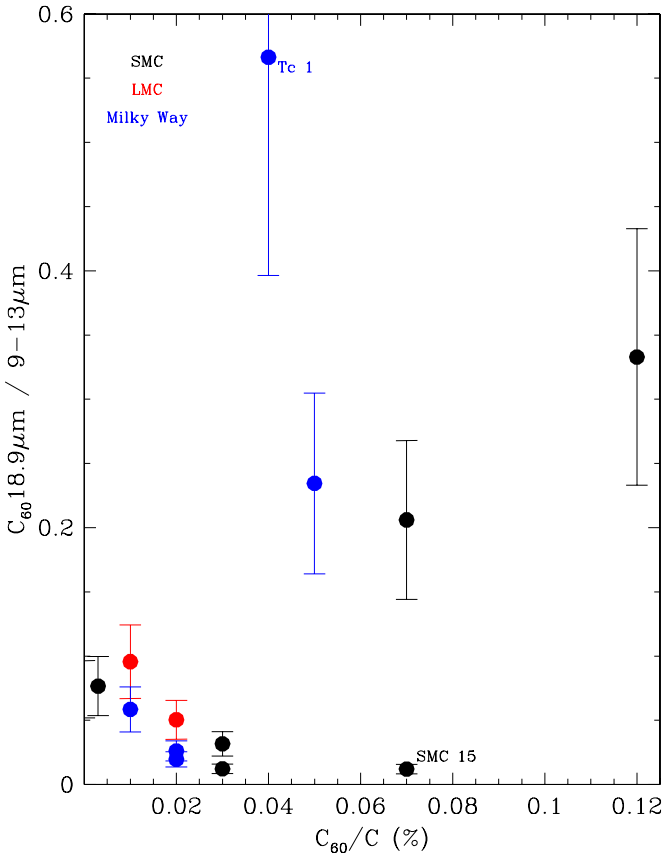

Figure 8. C_{60} 18.9 μm/9–13 μm flux ratio vs. the C_{60}/C abundance (in percentage) for fullerene PNe pertaining to different environments, such as the Galaxy and the Magellanic Clouds. Note that the apparent two outliers, Tc 1 and SMC 15, are indicated (see the text for more details).

(A color version of this figure is available in the online journal.)

[19] The only exceptions are LMC 02 and LMC 99, which have no significant 9–13 μm emission; see Figure 3.

in this diagram may involve a steeper correlation at the highest Galactic metallicities. However, Tc 1's *Spitzer* spectrum only covers the inner nebula, while the *Spitzer* apertures cover the full nebula in the rest of fullerene PNe displayed in Figure 8. On the other hand, SMC 15 displays the highest electron density ($N_e = 7500$ cm^{-3}) among the PNe in the SMC (with an average N_e of ~3500 cm^{-3}; see Table 2). It should be noted that by using the average electron density for SMC 15 (3500 cm^{-3}), a lower C_{60}/C abundance of ~0.03% is obtained. Thus, if we do not take into account Tc 1 and SMC 15, then Figure 8 would show an even tighter trend between the C_{60} 18.9 μm/9–13 μm flux ratio and fullerene abundances in fullerene PNe. In summary, we conclude that there is a tentative observed trend in Figure 8, but more detections of fullerenes in PNe are needed in order to reach a definitive conclusion.

More interesting is that Figure 8 may also be interpreted as a consequence of the destruction of the carrier of the 9–13 μm feature in those PNe dominated by the fullerene emission. This would be expected if the carrier of the broad 9–13 μm feature is a precursor of the fullerene molecules[20] and if it is intimately related with the fullerene formation process, as we have just interpreted in the previous section. As we have already mentioned in the Introduction, the strong variability of the broad 9–13 μm emission from source to source (see Table 4) is more consistent with an HAC identification.

Figure 9 compares the fullerene emission with the AIB emission at 6.2 and 11.3 μm (e.g., the C_{60} 18.9 μm/AIB 11.3 μm flux ratio versus the AIB 6.2 μm/AIB 11.3 μm flux ratio). We find two different groups in Figure 9. A first group composed of three PNe (Tc 1, LMC 02, and SMC 24),[21] which are dominated by the fullerene emission (C_{60} 18.9 μm/AIB 11.3 μm >8) and show very weak AIB emission at 6.2 and 11.3 μm (AIB 6.2 μm/AIB 11.3 μm < 0.75). These fullerene-dominated PNe are also characterized by the weakness of the broad 9–13 μm feature compared to the fullerene emission. This suggests that these three fullerene-dominated PNe may have a mix of aliphatic and aromatic hydrocarbon materials of similar chemical composition (e.g., size and degree of hydrogenation) and/or are under approximate physical conditions (e.g., the intensity of the UV radiation field) in their circumstellar envelopes. A second group in Figure 9, however, is formed by the rest of PNe in our sample that display similar levels of fullerene emission but covering a wide range of AIB 6.2 μm/AIB 11.3 μm flux ratios, likely reflecting quickly changing physical conditions (e.g., UV radiation field and/or the post-AGB shocks) and/or chemical composition. The latter is consistent with the relative strengths of the IR features of amorphous organic nanoparticles with mixed aliphatic and aromatic structures (e.g., HACs), which are known to be strongly dependent on physical conditions and chemical composition (e.g., Scott et al. 1997; Grishko et al. 2001). A similar result is obtained from Figure 10, where we display the C_{60} 18.9 μm/AIB 11.3 μm flux ratio versus the AIB 7.7 μm/AIB 11.3 μm flux ratio. Again, the same three fullerene-dominated PNe (although Tc 1 does not show the 7.7 μm AIB) form a separate group in this latter diagram, while the rest of objects show a wide range of AIB 7.7 μm/AIB 11.3 μm intensity ratios.

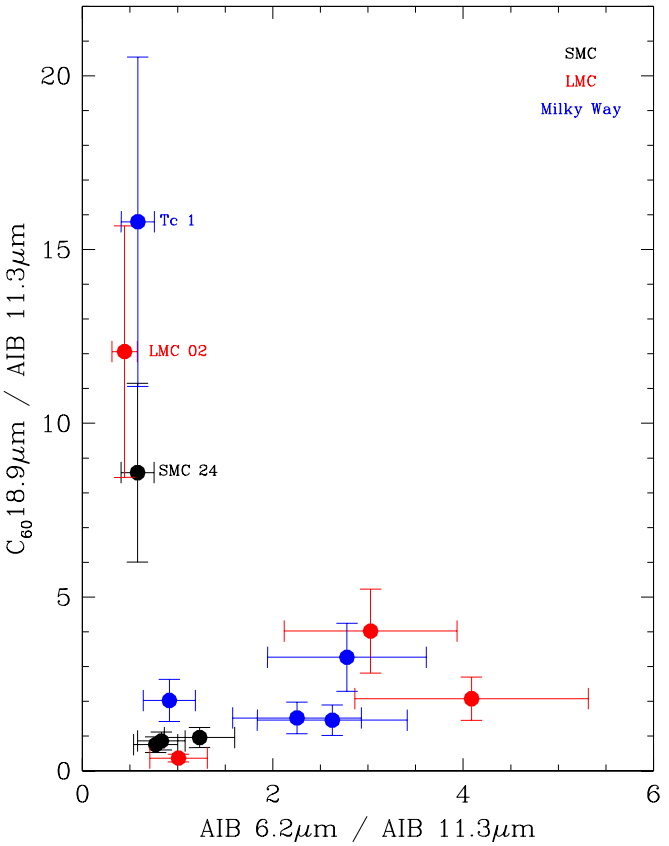

Figure 9. C_{60} 18.9 μm/AIB 11.3 μm flux ratio vs. the AIB 6.2 μm/AIB 11.3 μm flux ratio for fullerene PNe pertaining to different environments, such as the Galaxy and Magellanic Clouds. Note that several PNe are indicated.
(A color version of this figure is available in the online journal.)

Finally, a few MC PNe (LMC 25 and 48 in Figure 3 and SMC 13, 15, 18, and 20 in Figure 4) show a broad 15–20 μm emission (see also Table 4). This broad emission feature is usually attributed to the C–C–C bending modes of relatively large PAHs or PAH clusters (e.g., Van Kerckhoven et al. 2000). The 15–20 μm/11.3 μm and 15–20 μm/6.2 μm flux ratios are displayed in Figure 11 and they may be used to estimate the size (number of C atoms) of the grains/PAH clusters responsible for this emission (see, e.g., Van Kerckhoven et al. 2000; Tappe et al. 2006, 2012 for more details). All members of the 15–20 μm subgroup of MC PNe, with the exception of SMC 20, show AIB 11.3 μm/15–20 μm and AIB 6.2 μm/15–20 μm ratios lower than ~0.1 and 0.2, respectively, suggesting relatively large grains/PAHs clusters of more than 4000 C atoms (see Tappe et al. 2006, 2012, and references therein). Curiously, the observed characteristics of the 15–20 μm emission in these sources—shape, integrated strength relative to the 6.2 and 11.3 μm AIBs, and complete lack of the discrete emission features at 16.4, 17.0, and 17.8 μm—are very similar to the 15–20 μm bump observed in the shock-induced dust processing environment of the supernova remnant N132D (Tappe et al. 2006, 2012). Our interpretation is that these PAH clusters/amorphous carbon nanoparticles survive the harsh conditions in the circumstellar envelope long enough to be detected only in the low-metallicity environments of MC PNe. In our own Galaxy, however, the usual lack of PAH cluster-like 15–20 μm emission in fullerene PNe indicates that these PAH clusters/amorphous carbon nanoparticles are quickly destroyed.

[20] Note that the small amount of C_{60} (<1%; Table 3) is with respect to the total gaseous carbon in the nebulae. We do not know what fraction of carbon is locked in the carrier of the 9–13 μm feature. For example, if the 9–13 μm feature's carrier is of solid-state origin (dust), then only a small fraction of C (in comparison with gaseous carbon) is also expected for the 9–13 μm feature's carrier.

[21] Note that PN SMC 16 does not display the 6.2 and 7.7 μm AIBs and it would also pertain to this first group of fullerene-dominated PNe.

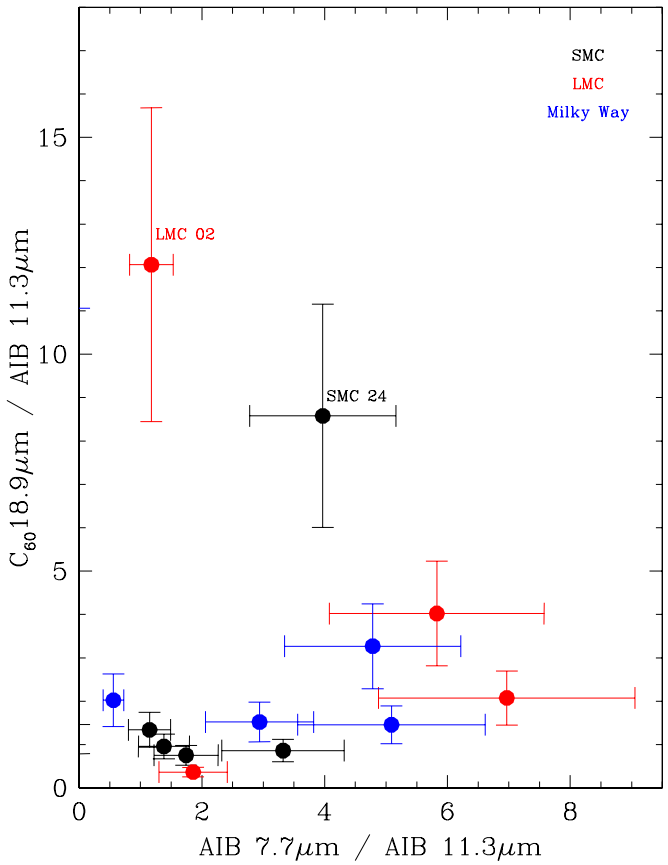

Figure 10. C_{60} 18.9 μm/AIB 11.3 μm flux ratio vs. the AIB 7.7 μm/AIB 11.3 μm flux ratio for fullerene PNe pertaining to different environments, such as our own Galaxy and the Magellanic Clouds. Note that several PNe are indicated.

(A color version of this figure is available in the online journal.)

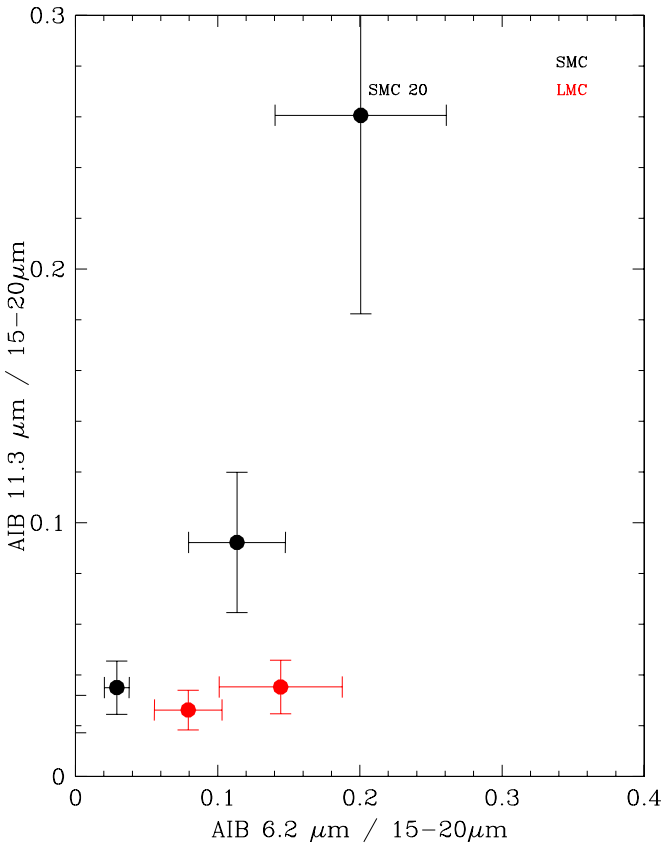

Figure 11. AIB 11.3 μm/15–20 μm flux ratio vs. the AIB 6.2 μm/15–20 μm flux ratio for fullerene PNe pertaining to the Magellanic Clouds. Note that PN SMC 20 is indicated.

(A color version of this figure is available in the online journal.)

4.5. Formation Route of Fullerenes in PNe

Some advances in our understanding of the fullerene formation process in PNe have been made since the discovery of C_{60} and C_{70} fullerenes in the PN Tc 1 by Cami et al. (2010). From the observational point of view, our recent detections of fullerenes and graphene precursors (possible planar C_{24}) in PNe have challenged our previous understanding on the formation of these complex molecules, showing that they can form in H-rich circumstellar environments and that they may coexist with PAH-like molecules (García-Hernández et al. 2010, 2011a). The coexistence of a great diversity of aromatic and aliphatic species in PNe with fullerenes supports the idea that fullerenes may form from the photochemical processing (e.g., as a consequence of UV irradiation or shocks) of small solid particles similar to that of HAC, the so-called HAC fullerene formation scenario. The prevailing view was that the H-poor RCBs, resembling the experimental conditions on Earth (Kroto et al. 1985), would be the ideal astrophysical environments for fullerene formation. However, *Spitzer* observations of RCB stars (García-Hernández et al. 2011b, 2011c) have shown that fullerene formation is inefficient in the highly hydrogen-deficient circumstellar environment of most RCBs. Fullerenes are seen in conjunction with strong PAH-like features in the two least H-deficient RCB stars DY Cen and V854 Cen. In addition, the V854 Cen's IR spectrum evolved from HACs to AIBs (e.g., from PAHs) and C_{60} in a timescale of only 10 years, supporting the "HAC fullerene formation scenario." The fact that previous *CLOUDY* photoionization models, using BB and Rauch (2003) stellar atmospheres as ionizing continuum, could not explain the low [Ne III]/[Ne II] ratios observed in fullerene MC PNe with fast stellar winds (e.g., shocks) prompted the speculation that fullerenes may be formed by the shock-induced decomposition of HAC material. This interpretation was consistent with the low effective temperatures (<25,000 K) found in the other astronomical environments, such as the proto-PN IRAS 01005+7910, post-AGB and RCB stars, and reflection nebulae, where fullerenes have been found so far (see below). The UV radiation field in the latter astrophysical environments is likely not intense enough for the photochemical processing of HAC (see discussion in García-Hernández et al. 2011b). Indeed, the PAH cluster-like 15–20 μm emission observed in fullerene PNe show a resemblance to that observed in the shock-induced dust processing environment of the supernova remnant N132D (Tappe et al. 2006, 2012).

However, the new *CLOUDY* models presented in this paper (Section 3.1) show that many of the observed [Ne III]/[Ne II] ratios may be explained by photoionization when using model atmospheres with line and wind blanketing. This result weakens the hypothesis of a shock-excited origin for the [Ne II] 12.8 μm emission. Although fast stellar winds (e.g., shocks) are generally present in fullerene PNe[22], the shock hypothesis cannot be directly tested with the actual data. Furthermore, the winds of central stars of PNe are radiation driven (Pauldrach et al. 1986)

[22] This is deduced from the common presence of P Cygni profiles in their UV lines (see also García-Hernández et al. 2011a).

and, as such, the wind velocity is expected to increase with the central star temperature, allowing the development of wind-driven shock regions when only the central star is sufficiently evolved (Villaver et al. 2002b). Weaker shocks are also expected to be associated with the propagation of the ionization front within the nebula. Figure 6 suggests that the UV radiation from the central star can explain the low [Ne III]/[Ne II] ratios observed in many fullerene PNe, putting some doubt on the suggestion of the fullerenes being formed by the shock-induced HAC's decomposition. In summary, this result, together with the narrow range of $T_{\rm eff}$ (∼30,000–45,000 K) displayed by our sample sources in Figure 6, indicates common fullerene formation conditions in PNe and suggests that perhaps the UV irradiation is photochemically processing the small solid particles with mixed aromatic and aliphatic structures similar to that of HAC dust and this process may form the fullerenes. This interpretation is consistent with the early suggestion by Kwok et al. (2001), who emphasizes the important role of photochemistry in the evolution from proto-PNe to PNe.

From the experimental point of view, we would like to emphasize the recent finding by Duley & Hu (2012) that HAC nanoparticles prepared under a variety of conditions can show IR features coincident with the four C_{60} IR features, which may be attributed to fullerene precursors or proto-fullerenes. The presence of proto-fullerenes takes place in conjunction with the 16.4 μm feature. This feature is usually present in the proto-PN IRAS 01005+7910, post-AGB and RCB stars, and reflection nebulae (all of them with $T_{\rm eff} < 30{,}000$ K), likely indicating the presence of proto-fullerenes (García-Hernández et al. 2012) as a previous stage in the evolution and dehydrogenation of UV irradiated HAC dust in fullerene PNe. More recently, Dunk et al. (2012) propose a Closed Network Growth (CNG) mechanism of fullerenes, where larger fullerenes may grow from pre-existing C_{60} molecules and this formation route can work under the presence of hydrogen. CNG of fullerenes would be consistent with the "HAC fullerene formation scenario" and it may work in the complex circumstellar environments of fullerene PNe. In this context, the smaller C_{50}, C_{60}, and C_{70} would be supplied by the photochemical processing of HAC dust.

5. CONCLUSIONS

In this paper, we present a detailed study of the *Spitzer* infrared spectra of 16 fullerene PNe. We report the first detection of fullerenes in the Galactic PN M 1−60 as well as the presence of an unusual set of infrared features at ∼6.6, 9.8, and 20 μm (attributed to possible planar C_{24}) in the PN K 3−54.

The observed C_{60} intensity ratios in the Galactic PNe with fullerene emission confirm our previous finding in the MCs that fullerenes—probably in solid state—in PNe are not excited by the UV radiation from the central star. In addition, new *CLOUDY* photoionization models show that line- and wind-blanketed model atmospheres can explain many of the observed [Ne III]/[Ne II] ratios using photoionization and that PNe-containing fullerenes display a rather narrow range in effective temperature (∼30,000–45,000 K). This shows that fullerene PNe share similar physical conditions for fullerene formation and that perhaps the UV radiation from the central star is processing the circumstellar dust grains—e.g., small solid particles containing aromatic, aliphatic, fullerene, and graphene structures similar to that of HAC dust—and forming fullerenes.

We have studied the fullerene emission with respect to other infrared emission features, such as the classical AIBs (usually attributed to PAHs) and the broad emission features at 6–9, 9–13, 15–20, and 25–35 μm, which we interpret as produced by a carbonaceous compound with a mixture of aromatic and aliphatic structures (e.g., HAC, coal, petroleum fractions, etc.) and/or their decomposition products (e.g., fullerene precursors or intermediate products). Thus, fullerenes and proto-graphene in PNe may be formed from the photochemical processing of such a carbonaceous compound, which should be very abundant in their circumstellar envelopes. Our interpretation is consistent with the early seminal work by Kwok et al. (2001).

The PNe targets that show fullerene emission belong to very different metallicity environments, such as our own Galaxy and the MCs. The detection rate of fullerenes in C-rich PNe is found to increase with decreasing metallicity, something that seems to be strongly linked to the limited dust processing in MC PNe when compared to Galactic PNe. It is important, however, to acknowledge the fact that all the original samples of PNe from which the fullerene detections come have their own selection biases and cannot be considered complete by any means. The fact that in general the *Spitzer* spectra of MC PNe are usually dominated by small dust grains (e.g., HAC and/or PAH clusters or even HAC decomposition products), while their Galactic counterparts display dust emission mainly from big grains (e.g., HAC aggregates), also points toward a higher probability of fullerene detection with decreasing metallicity under our proposed mechanism for fullerene formation. Our estimated fullerene abundances and temperatures are similar in the various metallicity environments analyzed. When possible, we have argued that fullerene PNe likely evolve from low-mass progenitors (main-sequence masses $<1.5\,M_{\odot}$) and are usually low-excitation objects slowly evolving towards the white dwarf stage.

We acknowledge support from the Faculty of the European Space Astronomy Centre (ESAC). D.A.G.H. and A.M. also acknowledge support for this work provided by the Spanish Ministry of Economy and Competitiveness under grant AYA−2011 − 27754. D.A.G.H. also thanks his son, Mateo, for his great patience during the final writing of the paper and C. Morisset for pointing out that the [Ne III]/[Ne II] ratios might be explained with models including line and wind blanketing. E.V. acknowledges the support provided by the Spanish Ministry of Science and Innovation (MICINN) under grant AYA−2010−20630 and to the Marie Curie FP7− People−RG268111. L.S. and R.A.S. acknowledges support by NASA through awards for programs GO 20443 and 50261 issued by JPL/Caltech. Thanks to James Davies for his help with the data analysis and to Susana Iglesias-Groth for the construction of the excitation diagrams. This work is based on observations made with the *Spitzer Space Telescope*, which is operated by the Jet Propulsion Laboratory, California Institute of Technology, under NASA contract 1407.

Facility: Spitzer (IRS)

REFERENCES

Acker, A., Raytchev, B., Stenholm, B., & Tylenda, R. 1991, A&AS, 90, 89
Becker, L., Bunch, T. E., & Allamandola, L. J. 1999, Nature, 400, 227
Bernard-Salas, J., Cami, J., Peeters, E., et al. 2012, ApJ, 757, 41
Bernard-Salas, J., Peeters, E., Sloan, G. C., et al. 2009, ApJ, 699, 1541
Boersma, C., Bauschlicher, C. W., Allamandola, L. J., et al. 2010, A&A, 511, 32
Buseck, P. R., Tsipursky, S. J., & Hettich, R. 1992, Science, 257, 215
Cahn, J. H., Kaler, J. B., & Stanghellini, L. 1992, A&AS, 94, 399
Cami, J., Bernard-Salas, J., Peeters, E., & Malek, S. E. 2010, Science, 329, 1180
Cataldo, F., Keheyan, Y., & Heymann, D. 2002, Int. J. Astrobiol., 1, 79
Chiappini, C., Górny, S. K., Stasińska, G., & Barbuy, B. 2009, A&A, 494, 591

De Vries, M. S., Reihs, K., Wendt, H. R., et al. 1993, Geochim. Cosmochim. Acta, 57, 933
Dopita, M. A., Meatheringham, S. J., Webster, B. L., & Ford, H. C. 1988, ApJ, 327, 639
Duley, W. W., & Hu, A. 2012, ApJ, 745, L11
Dunk, P. W., Kaiser, N. K., Hendrickson, C. L., et al. 2012, Nature Commun., 3, 855
Fabian, J. 1996, Phys. Rev. B, 53, 13864
Ferland, G. J., Korista, K. T., Verner, D. A., et al. 1998, PASP, 110, 761
García-Hernández, D. A. 2012, in IAU Symp. 283, Planetary Nebulae: An Eye to the Future, ed. A. Manchado, L. Stanghellini, & Schoenberner (Cambridge: Cambridge Univ. Press), 148
García-Hernández, D. A., Iglesias-Groth, S., Acosta-Pulido, J. A., et al. 2011a, ApJ, 737, L30
García-Hernández, D. A., Manchado, A., García-Lario, P., et al. 2010, ApJ, 724, L39
García-Hernández, D. A., Rao, N. K., & Lambert, D. L. 2011b, ApJ, 729, 126
García-Hernández, D. A., Rao, N. K., & Lambert, D. L. 2011c, ApJ, 739, 37
García-Hernández, D. A., Rao, N. K., & Lambert, D. L. 2012, ApJ, 759, L21
Gielen, C., Cami, J., Bouwman, J., Peeters, E., & Min, M. 2011, A&A, 536, 54
Girard, P., Köppen, J., & Acker, A. 2007, A&A, 463, 265
Grishko, V. I., Tereszchuk, K., Duley, W. W., & Bernath, P. 2001, ApJ, 558, L129
Henry, R. B. C., Kwitter, K. B., Jaskot, A. E., et al. 2010, ApJ, 724, 748
Herald, J. E., & Bianchi, L. 2004, ApJ, 611, 294
Herwig, F. 2005, ARA&A, 43, 435
Hony, S., Waters, L. B. F. M., & Tielens, A. G. G. M. 2002, A&A, 390, 533
Hrivnak, B. J., Volk, K., & Kwok, S. 2000, ApJ, 535, 275
Iglesias-Groth, S., Cataldo, F., & Manchado, A. 2011, MNRAS, 413, 213
Kaler, J. B., & Jacoby, G. H. 1991, ApJ, 372, 215
Kratschmer, W., Lamb, L. D., Fostiropoulos, K., & Huffman, D. R. 1990, Nature, 347, 354
Kroto, H. W., Heath, J. R., Obrien, S. C., Curl, R. F., & Smalley, R. E. 1985, Nature, 318, 162
Kwok, S. 2004, Nature, 430, 985
Kwok, S., Volk, K., & Bernath, P. 2001, ApJ, 554, L87
Kwok, S., & Zhang, Y. 2011, Nature, 479, 80
Leisy, P., & Dennefeld, M. 1996, A&AS, 116, 95
Leisy, P., & Dennefeld, M. 2006, A&A, 456, 451
Milanova, Yu. V., & Kholtygin, A. F. 2009, Astron. Lett., 35, 518
Morriset, C., Schaerer, D., Bouret, J. C., & Martins, F. 2004, A&A, 415, 577
Osawa, E. 1970, Kagaku, 25, 854
Pauldrach, A., Puls, J., & Kudritzki, R. P. 1986, A&A, 164, 86
Pauldrach, A. W. A., Hoffmann, T. L., & Lennon, M. 2001, A&A, 375, 161
Perea-Calderón, J. V., García-Hernández, D. A., García-Lario, P., Szczerba, R., & Bobrowsky, M. 2009, A&A, 495, L5
Pottasch, S. R., Surendiranath, R., & Bernard-Salas, J. 2011, A&A, 531, A23
Preite-Martínez, A., Acker, A., Koeppen, J., & Stenholm, B. 1989, A&AS, 81, 309
Rauch, T. 2003, A&A, 403, 709
Richer, M. G., López, J. A., Pereyra, M., et al. 2008, ApJ, 689, 203
Roberts, K. R. G., Smith, K. T., & Sarre, P. J. 2012, MNRAS, 421, 3277
Rubin, R. H., Simpson, J. P., O'Dell, C. R., et al. 2011, MNRAS, 410, 1320
Scott, A. D., Duley, W. W., & Pinho, G. P. 1997, ApJ, 489, L193
Sellgren, K., Werner, M. W., Ingalls, J. G., et al. 2010, ApJ, 722, L54
Shaw, R. A., Lee, T.-H., Stanghellini, L., et al. 2010, ApJ, 717, 562
Shaw, R. A., Stanghellini, L., Villaver, E., & Mutchler, M. 2006, ApJS, 167, 201
Speck, A., Corman, A. B., Wakeman, K., Wheeler, C. H., & Thompson, G. 2009, ApJ, 691, 1202
Stanghellini, L., García-Hernández, D. A., García-Lario, P., et al. 2012, ApJ, 753, 172
Stanghellini, L., García-Lario, P., García-Hernández, D. A., et al. 2007, ApJ, 671, 1669
Stanghellini, L., & Haywood, M. 2010, ApJ, 714, 1096
Stanghellini, L., & Kaler, J. B. 1989, ApJ, 343, 811
Stanghellini, L., Lee, T.-H., Shaw, R. A., Balick, B., & Villaver, E. 2009, ApJ, 702, 733
Stanghellini, L., Shaw, R. A., Balick, B., et al. 2003, ApJ, 596, 997
Stanghellini, L., Shaw, R. A., & Gilmore, D. 2005, ApJ, 622, 294
Stanghellini, L., Shaw, R. A., Mutchler, M., et al. 2002, ApJ, 575, 178
Stoy, R. H. 1933, MNRAS, 93, 588
Tappe, A., Rho, J., Boersma, C., & Micelotta, E. R. 2012, ApJ, 754, 132
Tappe, A., Rho, J., & Reach, W. T. 2006, ApJ, 653, 267
Tielens, A. G. G. M. 2008, ARA&A, 46, 289
Van Kerckhoven, C., Hony, S., Peeters, E., et al. 2000, A&A, 357, 1013
Vassiliadis, E., & Wood, P. R. 1994, ApJS, 92, 125
Villaver, E., García-Segura, G., & Manchado, A. 2002a, ApJ, 571, 880
Villaver, E., Manchado, A., & García-Segura, G. 2002b, ApJ, 581, 1204
Villaver, E., Stanghellini, L., & Shaw, R. A. 2003, ApJ, 597, 298
Villaver, E., Stanghellini, L., & Shaw, R. A. 2004, ApJ, 614, 716
Villaver, E., Stanghellini, L., & Shaw, R. A. 2007, ApJ, 656, 831
Volk, K., Hrivnak, B. J., Matsuura, M., et al. 2011, ApJ, 735, 127
von Czarnowski, A., & Meiwes-Broer, K. H. 1995, Chem. Phys. Lett., 246, 321
Zanstra, H. 1931, Z. Astrophys., 2, 1
Zhang, Y., & Kwok, S. 2011, ApJ, 730, 126